

Evolution of the Santa Cruz Mountains, California, through tectonic growth and geomorphic decay

Robert S. Anderson

Department of Earth Sciences and Institute for Tectonics, University of California, Santa Cruz

Abstract. I describe a strategy for modeling a specific large scale topographic feature that recognizes the discrepancy between tectonic and geomorphic scales and allows for important feedbacks between these processes. In the geomorphic model, the largest channel in each 4x4 km cell is explicitly treated, the channel incision being driven by a stream power rule. Hillslopes internal to each cell respond rapidly to incision of the local channel, prompting their treatment in the model as steady state forms. I present analytic expressions for the local relief, which is controlled by the local channel incision rate, and rate constants associated with the dominant hillslope process, either diffusive or landsliding. Initial conditions include any preexisting topography, and a lightly etched a channel network. The model is illustrated using the Santa Cruz Mountains, California. I show that an earlier hypothesis (that the Santa Cruz Mountains are due to advection of topography past an uplift source related to a restraining bend in the San Andreas Fault) remains viable when more specific geomorphic processes are considered. The local tectonics are represented by crustal thickening necessitated by conservation of mass in the bend, right-lateral translation of crust with respect to the bend, and flexural response to the distributed load. The model produces reasonable geographic and statistical distributions of topography using rates of tectonic and geomorphic processes that are within the range of those measured locally. This argues that this restraining bend is a long-lived feature of the San Andreas Fault. The slightly higher crest and shorter length of the southern Santa Cruz Mountains may potentially be explained by slightly faster slip of the crust west of the fault with respect to the bend than of that to the east. Deflection is minimal beneath these relatively small mountains, disallowing the interesting feedback of erosionally driven uplift. The predicted pattern of exhumation could be used to guide the search for fission track sites that could aid in the testing of the model.

Introduction

Modeling of large scale landscape evolution requires incorporation of realistic tectonic and geomorphic processes. The models should be capable of simulating changes in relief, which requires that both channel and hillslope erosion processes be included. The modeled lithosphere must respond through flexure to all rearrangements to surface loads, including either tectonic thickening or thinning of the crust, and to geomorphic rearrangements of mass. The models should be testable through measurement of geophysical, geologic and geomorphic information. The most difficult problem presented by a combined tectonic and geomorphic landscape evolution model is the discrepancy in temporal and spatial scales over which these processes operate.

While geologists and geomorphologists alike have long been interested in the evolution of mountain ranges, these differences in scale have led to compromises in characterization of either the tectonic or the geomorphic processes. Geomorphologists too often simplify tectonics to spatially uniform high uplift rates followed by stasis or to low and steady uplift rates, to drive erosion processes in a landscape. The first coupled models developed by geophysicists, while using elegant tectonic algorithms, tended to reduce geomorphology to a buzz saw or to some other simplified set of rules.

Copyright 1994 by the American Geophysical Union.

Paper number 94JB00713.
0148-0227/94/94JB-00713 \$05.00

Molnar and England [1990] highlight the need for models in which geomorphology and tectonics are appropriately taken into account. They emphasized that enhanced relief caused by rapid incision of valleys during climate degradation and alpine glaciation leads to flexural uplift of rock in major mountain ranges. The possibility that the maximum elevations in a range can therefore increase while the mean elevation decreases has important implications on both local and regional scales. Precipitation from air masses forced over the maximum elevations of a range can set up an orographic feedback on geomorphic processes, further enhancing the relief. In addition, the mountain range poses a barrier to flow that alters circulation patterns on a regional scale [Raymo *et al.*, 1988; Ruddiman and Kutzbach, 1989]. Models capable of addressing these feedbacks must therefore simulate both the production of relief within a range, and the flexural response to the distributed load; both geomorphology and geophysics are needed.

Geomorphic modeling in the 1980s, following the pioneering work of Culling [1960, 1965] and Ahnert [1970], was dominated by attempts to understand smaller-scale landform evolution. In particular, several teams addressed the diffusional relaxation of scarps, marine terraces, and beach ridges [e.g., Nash, 1980; Hanks *et al.*, 1984; Andrews and Hanks, 1985; Pierce and Colman, 1986; Andrews and Bucknam, 1987]. Models of fluvial systems focused on the details of individual meanders or on the response of alluvial systems to changes in base level [e.g., Chappell, 1974; Begin, 1988]. While much progress has been made, the small scales addressed in these models render them incapable of incorporating tectonics at the crustal scale.

Tectonics is relegated to only the crudest of roles, e.g., in determining the base level of the stream or hillslope system.

Stein *et al.*, [1988] and King *et al.* [1988] have recently proposed that mountain scale topography could be produced by the repetition of crustal dislocations on faults. They couple elastic deformation associated with coseismic and postseismic slip, geomorphic beveling of topographic highs, and long-term isostatic adjustment to the evolving load to produce mountain ranges in a variety of tectonic settings. While their tectonic model showed considerable sophistication, and could be constrained by a variety of geodetic techniques, their treatment of geomorphic processes was crude. Mass was moved from high places and placed in adjacent lows. Because the models were two-dimensional (2-D), in order to accommodate depositional systems running along the range front, depositional mass was at times much greater than erosional mass.

Working instead on a 2-D planform grid, Koons [1989] coupled a realistic specified uplift pattern with a set of rules describing the geomorphic system that included both diffusive processes and channel incision to produce a model of New Zealand's southern Alps. He succeeded in reproducing the essence of the ridge pattern dominating the shape of the range. Yet the rules used to represent geomorphic processes were not physically based. The channels were simply draped into the topography with longitudinal profiles scaled by the elevation difference between the ridge crests and the sea. The grid using 1x1 km cells was then diffused. Other geomorphic processes such as landsliding, and all activity associated with smaller order drainages, were subsumed in the topographic diffusivity. In order to attain realistic ridge line heights, diffusivities many orders of magnitude higher than those measured in any landscape to date were demanded by the model.

More recently, a number of researchers have advanced models addressing landscape evolution at moderate to large scales [e.g., Willgoose *et al.*, 1991; Chase, 1992; Beaumont *et al.*, 1992; Kooi and Beaumont, 1994; Tucker and Sligerland, 1994]. All such models operate upon a gridded landscape using a set of rules that attempt to capture the essence of the various geomorphic processes acting. They differ significantly in strategy, Chase [1992] using the collective action of a set of events ("precipitons"), others using finite difference approximations to differential equations meant to mimic long-term average processes. A principal distinction between these models and those addressing smaller scales is that at small scales the diffusion model describes well the processes operating locally on hillslopes, where the relevant parameters such as soil production rates and diffusion coefficients can be measured in the field [e.g., Monaghan *et al.*, 1992; McKean *et al.*, 1993]. At large scales, however, the processes are not necessarily diffusive. The cell sizes in the large landscape evolution models are commonly many times the length of individual hillslopes in the real landscape they are meant to simulate. The effective diffusivities necessary to ensure that the resulting model elevations remain reasonable are commonly many times those measured in the field.

One purpose of this paper is to present a model strategy that diverges from other models principally in how it deals with the scale mismatch. I present a simple, computationally compact 2-D planform model that contains the essence of the tectonic and geomorphic processes operating at the mountain range scale. I try to remain faithful to the scales at which these processes act and propose a potential but certainly nonunique solution to the severe mismatch in scales at which the tectonic and the geomorphic processes act. The model also permits a flexural response of the crust.

I illustrate the model by applying it to the Santa Cruz Mountains in California's coast ranges (Figure 1). I build upon the hypothesis put forth in earlier work [Anderson, 1990] that the Santa Cruz Mountains are produced by advection of crust past an uplift source associated with a restraining bend in the San Andreas Fault. On either side of the fault, crust translating toward the bend thickens due to contractile areal strain, a portion of this thickening resulting in rock uplift. The rock mass is attacked by geomorphic processes that both create relief and reduce the mean surface uplift rate to below that of the rock uplift rate. Once beyond a position at which the tectonically driven rock uplift rate falls below the geomorphic lowering rate, the mean surface elevation declines as the crust translates further.

The second purpose of this paper is therefore to demonstrate that this hypothesis, which was supported earlier principally by scaling arguments, remains viable even when more detailed tectonic and geomorphic processes are embedded in a numerical model of the topographic evolution. Since the earlier work, the medium term uplift rates have been better constrained [Anderson and Menking, 1994; Valensise and Ward, 1991], as have the geomorphic processes and rates within the terraced fringe of the topography [Rosenbloom and Anderson, 1994].

The model space is gridded into 4x4 km pixels, a scale sufficiently small to allow resolution of the tectonic forcing and significantly larger than first-order drainages. The long-term

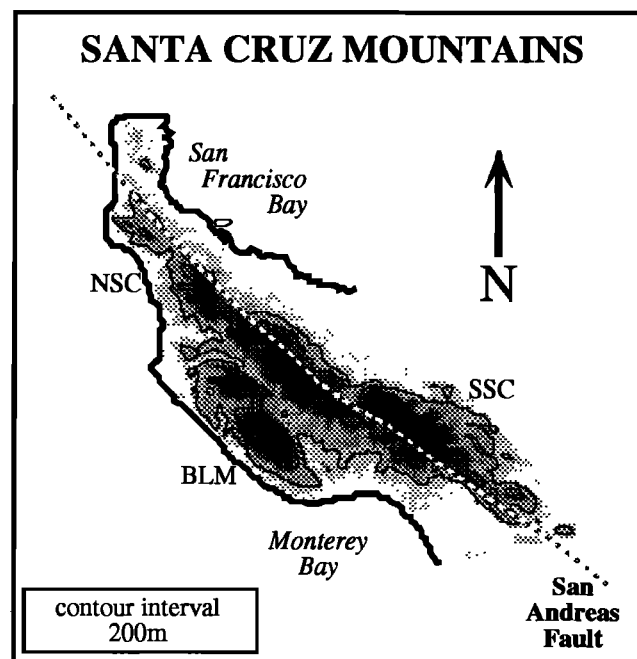


Figure 1. Santa Cruz region topography, shown from the 5 arc sec digital elevation model (0.925 km spacing). Also shown is the San Andreas Fault with its associated bend within the Santa Cruz Mountains, breaking the mountains into a northern range (NSC) to the west of the fault and southern range (SSC) to the east. Maximum elevations are roughly 1 km in both ranges, Loma Prieta (1100 m) on the southern crest and Mount Bielawski (900 m) on the northern crest. Also labeled is Ben Lomond Mountain (BLM), a gently sloping massif separated from the remainder of the NSC range by prominent drainages (see Figure 4). Together, these ranges comprise the spine of the San Francisco peninsula and separate Monterey Bay from San Francisco Bay.

uplift rate pattern is determined by the pattern of crustal deformation associated with a restraining bend. Slip of both sides of the San Andreas Fault with respect to the bend is imposed. An initial channel network is assumed to etch, without planview deformation, into the uplifting rock mass. Only the largest of the channels in each cell is treated explicitly. The hillslopes and smaller-order tributaries are not explicitly calculated. Instead, hillslopes are parameterized using subsidiary calculations that connect the local relief (ridge crest minus channel elevation) and average elevation of a hillslope to channel incision rate. Both landsliding and diffusive hillslope processes are allowed and are tied to a threshold channel incision rate.

The properties of the system reported by the model include geophysical fields that can be used to test this and other models. I have tried to maintain connection to measurable properties of the system, both through using geomorphic rates that are measurable in the field and through predicting from the model such quantities as the spatial distribution of the exhumation field at any time and the exhumation histories of points within the range.

I first outline the topographic and tectonic settings of the Santa Cruz Mountains. I then develop mathematical descriptions of the tectonic and geomorphic processes that are coupled to become the topographic evolution model. A simple subgrid calculation is performed, from which I calculate the inherent timescales in the geomorphic system, which in turn justify the parameterization of the smaller scale processes. The results of the full model take the form of maps of a variety of fields, all presented on a 4x4 km mesh, including rock uplift, mean topography, exhumation, relief, and flexural deflection. I also present histories of elevation, relief, exhumation, and flexural deflection following a parcel of crust.

The Topographic Setting

Large Scale

The Santa Cruz Mountains straddle the San Andreas Fault (Figure 1), the northern half of the range being largely west of the San Andreas, the southern half to the east. The range is roughly 100 km long along the strike of the fault and 40 km wide normal to the strike of the fault. Maximum altitudes of both ranges are roughly comparable: the ridge Loma Prieta crowns in the southern range reaches 1130 m, while Mount Bielawski in the northern range is 985 m tall. The hypsometry of the range shown in Figure 2 may be used to calculate a mean elevation of about 240 m, ignoring the broad alluvial apron of the southern San Francisco Bay area below 20-m elevations.

While the southern range is one contiguous mass with width of about 15 km, the northern range is considerably wider. Much of the enhanced width comes from the isolation of a second, more western crest in Ben Lomond Mountain (Figure 1), a gently seaward sloping ramp separated from the range crest by the headwaters of the San Lorenzo and Pescadero drainages. The mean width of the northern range is roughly 30 km.

Small scale

The ranges are bordered on the west by coastal terraces and on the east by a depositional environment characterized by alluvial fan complexes. Sediment is rapidly transported away from the mountain range on the west, as southeasterly longshore drift efficiently transports sediment to the throat of the Monterey Canyon. In contrast, sediment is trapped in the topographic basin in the southern San Francisco Bay and is kept relatively close to the source region. The resulting alluvial fans and bay muds together comprise a low relief surface with 0–2° gradients.

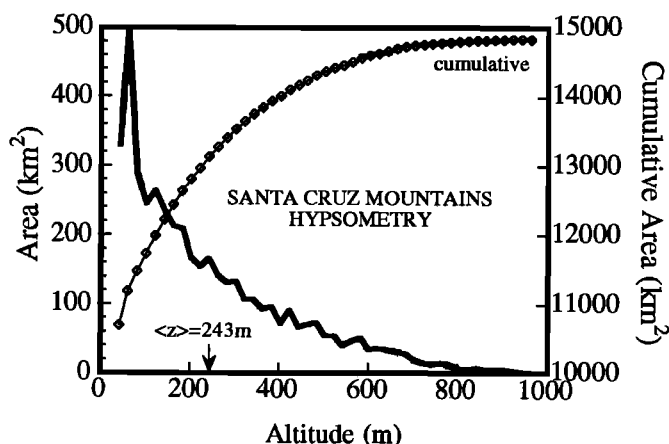


Figure 2. Santa Cruz Mountains hypsometry, showing a characteristic decline in area with increasing elevation. The mean elevation of the range is only 240 m, ignoring the area below roughly 10 m that dominates the fringe of the San Francisco Bay area. Also shown is the cumulative hypsometric curve (area below a specified elevation), which does include this area.

The bulk of the range consists of high relief topography with large slope angles. Representative slope profiles are shown in Figure 3 sampled from near the crest of the southern Santa Cruz Mountains. Note the consistent approach to a straight long steep slope, a typical average gradient being roughly 1:2 (26°). Landslides and debris flows in the mountains are common [e.g., *Griggs et al.*, 1990]. The drainage pattern of the range is shown in Figure 4. The largest streams draining to the west coast are the San Lorenzo and Pescadero Rivers, which wrap behind Ben Lomond Mountain to drain both its back side and the west slope of the northern crest.

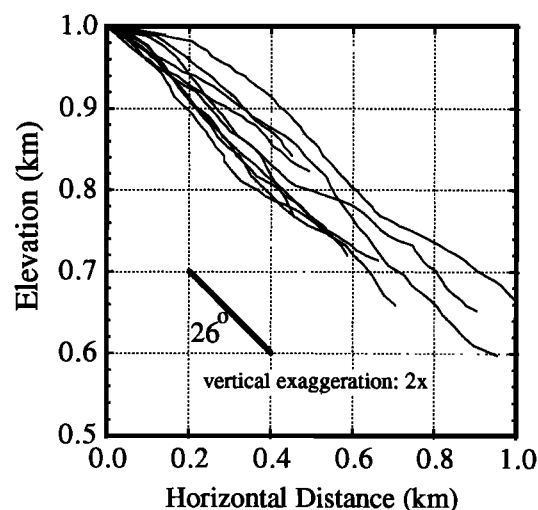


Figure 3. Hillslope profiles within the crest region of the Santa Cruz Mountains, digitized from U.S. Geological Survey (USGS) quadrangles at 20 foot (Chittenden Quadrangle) and 40 foot (Los Gatos Quadrangle) vertical spacings. Note the relatively straight long slopes and the convex tops to some of the ridges. Many of the ridges show little rounding at all at this map scale, implying the diffusive processes are overwhelmed by landsliding. While there are clearly anomalously high slopes in places (in part due to digitizing resolution), the mean slope angles appear to be roughly 1:2, or 26°.

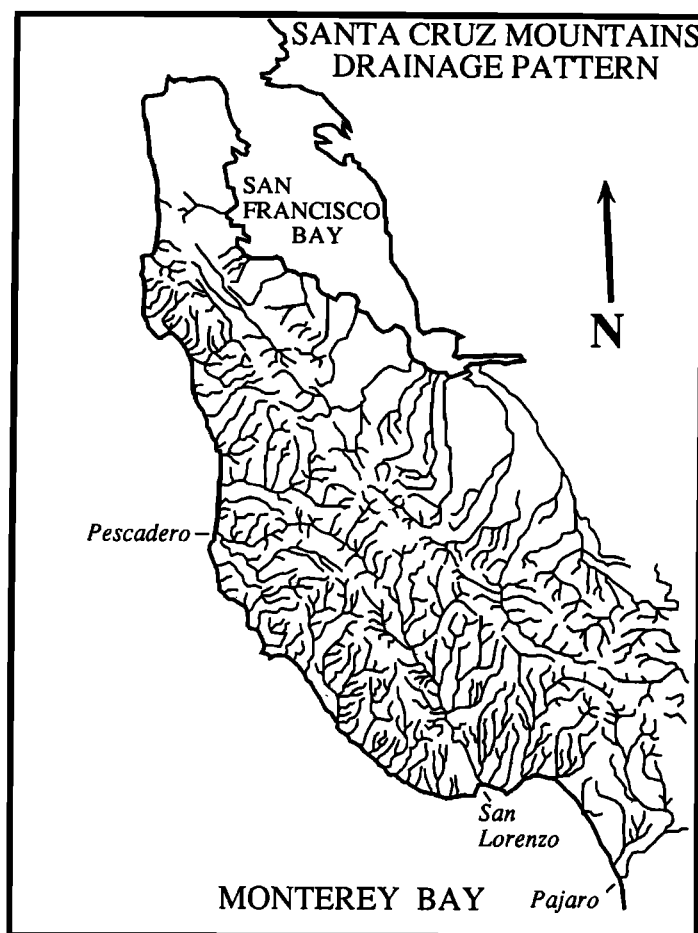


Figure 4. Drainage network in the Santa Cruz Mountains, derived from 1:100,000 map. The two most significant drainages toward the west are the San Lorenzo River and Pescadero Creek, which drain the back side of Ben Lomond Mountain, the prominent subsidiary western massif shown in Figure 1.

Climate

The geomorphic processes and their intensities vary within the region due to both the position of a particular parcel of landscape within the uplift pattern and to microclimatic variations. The present climate is Mediterranean, with the majority of the precipitation arriving between October and April in storm systems with westerly trajectories. Annual rainfall varies from 70 to 200 cm and is highly modified by orographic effects [Rantz, 1971]. Rainfall varies roughly linearly with elevation from the coast to the crest of Ben Lomond Mountain. The crest of the central Santa Cruz Mountains lies in the rain shadow of Ben Lomond Mountain and therefore displays a smaller precipitation maximum. The resulting vegetation is dominated by grasslands at low elevations and redwood forests above about 200 m.

Tectonic and Geophysical Processes

Formulation of the tectonically produced vertical strain associated with advection past a stationary uplift source requires specification of the uplift pattern, and of the velocity of a parcel of crust with respect to the source (see Figure 5). The elevation z at a point (x, y) , x taken parallel to the fault in the direction of motion of the crust, may be written

$$\frac{\partial z}{\partial t} = \frac{Dz}{Dt} - U \frac{\partial z}{\partial x} \quad (1)$$

where $\partial z / \partial t$ represents changes in elevation within a fixed reference frame, Dz/Dt , the total derivative, represents changes in elevation following a material point, and U is the horizontal velocity in the x -direction. Gradients in topography in the direction of the motion, $\partial z / \partial x$, result in changes in elevation at a fixed point within the fixed reference frame; i.e., the second advective term plays a role.

Following a parcel of crust as it moves along the fault, changes in elevation will result from local thickening or thinning of the crust due to tectonic and geomorphic processes and from isostatic adjustment to the altered regional distribution of surface and subsurface loads. It is through the large length scale associated with the flexural adjustments that local generation of relief can drive regional uplift. The tectonic description of the system must therefore include the slip rates, an uplift pattern representing the tectonic thickening of the crust, and the flexural response to distributed surface and subsurface loads.

Slip Rates

The slip rates on the San Andreas Fault in the Peninsula segment north of the region of the bend are estimated to be 19 ± 4 mm/yr [e.g., Working Group on California Earthquake Probabilities (WGCEP), 1990; Bilham and Bodin, 1992]. Geologic constraints based upon offset marine embayments and distinctive clasts displaced from their source terrain place 2–4 Ma averaged slip rates between 10 and 20 mm/yr [Brown, 1990].

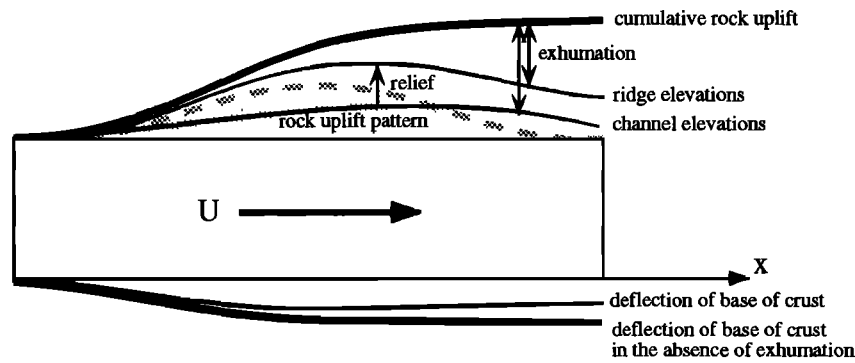


Figure 5. Schematic 2-D evolution of a parcel of crust as it translates through a stationary region of uplift, here stippled. Cumulative thickening represents the integral of the vertical strain experienced at any point; some of the thickening results in rock uplift; some results in isostatic growth of a root. Geomorphic attack of the topography results in a roughened surface with relief corresponding to the difference between maximum (ridge crest) and minimum (channel) elevations. The mean elevation at any point will be intermediate between the maximum and minimum and will be dependent upon the shapes of the hillslopes. Exhumation measures the difference between the local topographic surface and the cumulative rock uplift surface that would have defined the topography in the absence of geomorphic attack.

Holocene slip rates on the Peninsula segment are unexpectedly low, at 12 mm/yr [Hall, 1984], although these figures are currently being re-evaluated.

Uplift Rates and Patterns

I first argue that conservation of mass in a fault bend sets a constraint on the integral of the uplift rate. Then I assess the roles of individual structures in accomplishing the vertical strain. In this strike-slip setting, over the timescales considered in this model, these structures migrate out of the bend, and I rely instead upon a generalized vertical strain pattern associated with the large scale San Andreas Fault geometry.

Long-Term: Conservation of Mass in a Strike-Slip Fault Bend

Consider a slight bend in a right-lateral strike-slip fault across which the relative velocities are U_{rel} (Figure 6). We wish to determine the expected mean rate of thickening in the region surrounding the bend. The bend has length λ and a divergence angle from the adjacent straight reaches of the fault, θ . We assume that mass must be conserved above a basal detachment layer in either the lower crust or upper mantle, a depth H below the surface. The rate of mass arrival in the bend region from both sides of the fault is

$$\dot{M} = \rho H \lambda \sin(\theta) \{ (U_{rel} - U) + U \} = \rho H \lambda U_{rel} \sin(\theta) \quad (2)$$

where ρ is the mean crustal density.

For the scale of bend and divergence angle considered here, we expect that the mass is accommodated through thickening in an area A , rather than through either significant changes in density, or to detachment of lithospheric mantle at depth. The dimensions of this accommodation area will be scaled by the bend length λ and the crustal thickness H . For simplicity, we take the fault-parallel length scale to be $\lambda + 2\beta H$, where β is a parameter of order 1 and the factor 2 comes from tip regions on either side of the bend. Similarly, the fault-normal length scale will be $2\beta H$. The parameter β will be dependent upon the strength of the crustal materials, small β corresponding to weak materials in which the deformation associated with the bend is accommodated in a slim

region nearby the fault, large β corresponding to a broad region of deformation. Under the assumption of constant crustal density, the areally averaged thickening rate must then be $\dot{M}/\rho A$, or

$$\langle \dot{H} \rangle = U_{rel} \lambda \sin(\theta) / (2\beta (\lambda + 2\beta H)). \quad (3)$$

The calculated mean thickening rate for the Santa Cruz bend on the San Andreas Fault (SAF) is therefore roughly 0.7 mm/yr, given $U_{rel} = 20$ km/m.y., $\theta = 8^\circ$, $\lambda = 50$ km, $H = 25$ km, and taking $\beta = 1$. Note that this is the mean thickening rate over the area A and that the maximum thickening rates should be significantly higher than this.

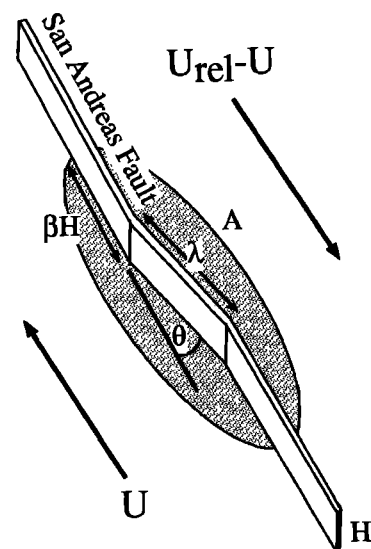


Figure 6. Schematic geometry for calculation of thickening within a bend in a right lateral strike slip fault. The bend is characterized by an opening angle θ and a length λ . Depth of the master fault is H . Relative slip across the fault, U_{rel} , is partitioned into slip U of the west side of the fault with respect to the bend, and $U_{rel} - U$ of the east side with respect to the bend. The thickening is taken up over a region A , which will be scaled by the wavelength of the bend and by some length normal to the fault that will scale with H , here βH .

Note that in addressing the evolution of the mountains adjacent to such a bend, it is insufficient to specify the relative motions across the fault. The important parameter is the relative velocity of a particular parcel of crust with respect to the bend (or uplift source). If one side of the fault is much more rigid than the other, the bend may be considered part of the rigid side, and all the deformation will be taken up by the weak crust on the other plate. Studies of offset features across the fault yield only relative displacements across the fault, not displacements with respect to the bend. The topography plus exhumation, representing the total vertical strain of a parcel of crust, should on the other hand reflect the relative displacement with respect to the uplift source associated with the bend.

Uplift Mechanisms

Uplift along a strike-slip fault is caused by areal strain associated with gradients in slip and with geometric complexity along the fault. Considering a crustal slab of thickness H and assuming the problem to be one of plane stress, the thickening may be calculated through $\Delta H = H[-\nu/(1-\nu)](\epsilon_{xx} + \epsilon_{yy})$, where ν is Poisson's ratio and the strains are the horizontal linear strains [Bilham and King, 1989]. The thickening will be scaled by the divergence angle of the fault bend, the crustal thickness, and Poisson's ratio. For an 8° fault bend the maximum thickening strain, $\epsilon_z = \Delta H/H$ is of the order of 0.075 for a fault displacement of 10% of the bend length, conserving mass by using $\nu = 0.5$ [Bilham and King, 1989]. Converting this to thickening rates requires knowing the total thickening, $\epsilon_z H$, and the time elapsed in accomplishing the 10% slip, $\tau = 0.1 \lambda U_{rel}$. In the Santa Cruz bend case, this corresponds to maximum thickening rates of about 0.75 mm/yr, using a slip rate U_{rel} of 20 km/m.y., plate thickness of 25 km, and bend length of 50 km. This value is in rough accord with the calculation above considering conservation of mass. The details of the pattern of uplift are, however, determined by the specific structures accommodating the areal strain.

Role of Fault Structures

The specific structures within the crust allowing the vertical strain associated with a fault bend will vary through time. The material being strained is not a perfectly elastic medium. Rather it is cut by discrete faults across which displacement is permanently accommodated. The short-term uplift pattern should therefore be dictated by these faults. In the Santa Cruz Mountains, the San Andreas Fault (SAF) accomplishes the majority of right-lateral translation. Other active fault structures appear to include the east dipping Loma Prieta structure and a complex of frontal thrusts to the east of the southern Santa Cruz Mountains crest [see Burgmann et al., this issue; McLaughlin et al., 1988]. Repeated events on the Loma Prieta structure can well explain the elevations of the marine terraces along the coast of the northern Monterey Bay [Anderson, 1990; Anderson and Menking, 1994]. The Loma Prieta uplift pattern can explain much of the recent (order 100–500 kyr) uplift to the west of the SAF. Anderson and Menking [1994] calculate long-term average recurrence times of roughly 300–550 years for Loma Prieta events, based upon the inferred number of coseismic events, the ages of the marine terraces, and the Loma Prieta coseismic slip parameters determined by geodetic techniques [Lisowski et al., 1990] of 1.7 m dip slip and 2.2 m right lateral slip on a 75° dipping rupture plane. Given the maximum coseismic uplift of approximately 550 mm [Lisowski et al., 1990; Marshall et al., 1991; Williams et al., 1993], this recurrence interval translates into 1.0–1.8 mm/yr

uplift due to repeated Loma Prieta events. This is sufficient to accomplish the vertical strain on the west side of the SAF, implying that the Loma Prieta structure is the principal actor at present.

However, as has been noted [Schwartz et al., 1990; Anderson et al., 1990], repetition of Loma Prieta events would lead to the long-term lowering of the crest of the southern Santa Cruz Mountains, to the east of the SAF. The operation of other uplift mechanisms is therefore implied, the most likely candidates being west dipping frontal thrusts with traces to the east of the crest. No seismic events have been documented that have resulted in a positive change in elevation on Loma Prieta. Yet the steep terrain and the visibility of the fault traces of the Sargent, Shannon, Berrocal and other faults argue for recent activity on these structures. The relative timing of such faulting is not resolved. We do not know whether the Loma Prieta and eastern frontal systems are operating simultaneously, trading off events or whether the Loma Prieta structure operates for tens of thousands of years before switching back to the eastern frontal system. There are no convenient natural long-term bench marks on the east side of the mountains to record this history.

Given that a parcel of crust will spend of the order of 4–5 m.y. in the bend, it is likely that particular compression-accommodating structures like the Loma Prieta fault will grow and die as they move into and out of the region of greatest strain and as they rotate within the strain field. We cannot document all the faults that might have been active in the course of the 8–10 m.y. since the triple junction passed this latitude [Irwin, 1990]. In summary, the short-term uplift pattern will be dictated by the uplift associated with these specific structures, the long-term pattern must take into account all structures operating through the lifetime of the bend. We may constrain the integral of the uplift by appeal to conservation of mass within the bend region.

Generalized Strain Associated with the Bend in the San Andreas Fault

I have therefore opted to use a simple uplift pattern that roughly mimics the expected long-term vertical strain field. I have chosen the relevant bend to be the 40–50 km long Santa Cruz bend with which the Loma Prieta structure is currently associated. This bend has the largest divergence angle in the region, and therefore ought to result in the largest uplift rates. I approximate the uplift as shown in Figure 7 with a Gaussian dome of magnitude 1 mm/yr, horizontal scale length parallel to the fault of 15 km, and scale length normal to the fault of 15–20 km. The latter roughly fits the cross section of patterns generated using a 3-D boundary element code [Gomberg and Ellis, this issue]. The scale for the uplift rate, which is adjustable in the model, is constrained by arguments made above concerning (1) conservation of mass in a bend; (2) uplift rates associated with repeated Loma Prieta events; and (3) vertical strain associated with areal contraction in a fault bend as reported by Bilham and King [1989].

Deflection

The evolving region of uplifted topography constitutes a distributed load on the lithosphere, which therefore deforms at long wavelengths. It is this flexure, which acts to hide some of the thickening of the crust due to tectonic processes or acts to produce uplift due to relief-creating geomorphic processes, that must be incorporated to allow for Molnar and England's [1990]

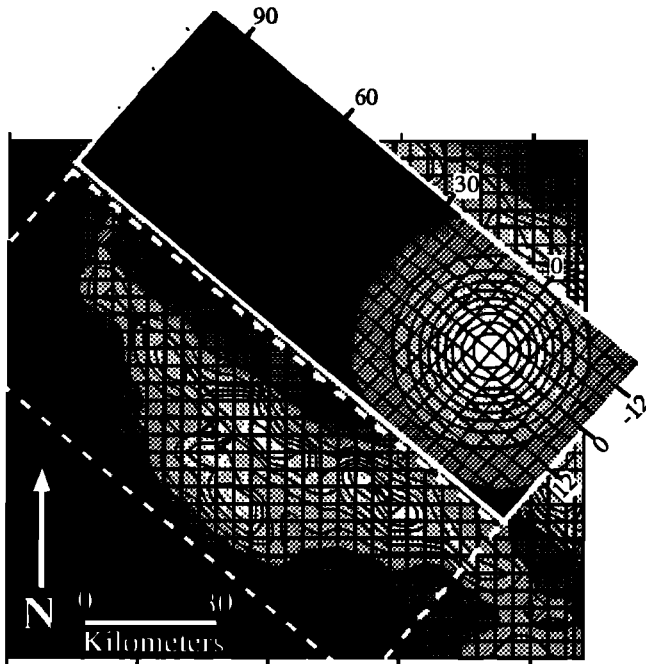


Figure 7. A sample of the uplift pattern used in the topographic calculations, here as in all subsequent plots of model output shown against a backdrop of the actual topography averaged in 4x4 km grid boxes. The model space is shown shifted NE from the topography it is meant to depict, shown in the dashed white box. The uplift pattern is depicted with a 0.1 mm/yr contour interval, here with maximum uplift rate of 1 mm/yr. The pattern is a Gaussian dome, with width normal to and parallel to SAF prescribed in the model (here shown equal). The center of the uplift pattern is placed at (0,0) in the model space and corresponds to the center of the Santa Cruz bend, or roughly the epicenter of the Loma Prieta earthquake.

proposed feedback. The topographic load is supported by a combination of buoyancy, and fiber stresses set up within the bent elastic portion of the lithosphere [e.g., *Turcotte and Schubert*, 1982]. The buoyancy forces are proportional to the density difference between the materials in the subsurface and to the amplitude of the deflection of the interface between such materials. This acts as a restoring force to any attempted deflection of the interface. Flexure of the elastic portion of the lithosphere is otherwise controlled by the elastic properties of Young's modulus E and Poisson's ratio ν and by the effective elastic thickness of the plate, H . This latter vertical length scale is the most difficult to constrain. It is arguably controlled by the thermal state of the upper crust [e.g., *McNutt*, 1990]. Several workers in the western United States [e.g., *Stein et al.*, 1988] have used widths of geological structures to constrain the effective elastic thickness to be of the order of 5-10 km. The relevant horizontal length scale in the problem is the flexural parameter α :

$$\alpha = \left(\frac{D}{\rho_d g} \right)^{1/4} \quad (4)$$

where ρ_d is the density of the ductile material, and D is the flexural rigidity:

$$D = \frac{EH^3}{12(1-\nu^2)} \quad (5)$$

The flexural parameter D scales the radius within which a point load will cause an appreciable deflection.

While formulations for the deflection due to a specified line load are simply cast [*Turcotte and Schubert*, 1982], and such solutions may be linearly superimposed to reflect simple 2-D loads, the topographic loading as associated with realistic mountains is a complicated 2-D pattern, primarily due to the large scale channels draining a mountain range. It is important to incorporate the effect of channel-incised relief in order to trigger the feedback described by *Molnar and England* [1990]. I therefore use a deflection model obtained by summing deflections associated with point loads at each grid node. *Lambeck* [1988] shows the deflection w at a nondimensional distance r/α due to a point load at radial distance $r=0$ to be:

$$w\left(\frac{r}{\alpha}\right) = \frac{q}{2\pi\rho_d g \alpha^2} \text{Kei}\left(\frac{r}{\alpha}\right) \quad (6)$$

where q is the point load, and Kei is the Kelvin function, which behaves as a highly damped sinusoid. Deflection at any point within a gridded model domain is therefore calculated by summing contributions to flexure from all cells within the calculation space. The loads q are sums of surface and subsurface loads. The surface load associated with subaerial topography, taken positive downward, is $z g (\rho_e - \rho_a) dx dy$, while the subsurface load associated with a low-density root is $\Delta z_d g (\rho_e - \rho_d) dx dy$, where g is the acceleration due to gravity, z is the altitude of the grid node, Δz_d is the amplitude of the deflection of the subsurface density-contrast interface, dx and dy are the horizontal dimensions of the model grid cells, and ρ_a , ρ_e , and ρ_d are the densities of air, elastic crust, and ductile lower crust, respectively. Contributions to deflections from loads outside the calculation space are ignored.

Geomorphic Processes

I combine crude models of stream incision and hillslope processes in an algorithm for the geomorphic attack of the rising mountain ranges. One should not expect to be able to model the evolution of the topography of a mountain range with diffusive processes alone. As *Koons* [1989] demonstrated convincingly, the incision of channels into the bedrock of the rising mountain range is essential in setting the boundary conditions for the surrounding hillslopes. One must therefore posit a rule set for the channels, and a rule set that efficiently describes the response of the adjacent hillslopes.

The geomorphic system is characterized by several different timescales. In order of increasing response time, these are associated with (1) hillslope profiles, (2) channel longitudinal profiles, and (3) the planview pattern of the drainage system. Once set into the landscape through a complicated and historically unique set of initial conditions, we expect the channel planview pattern to remain essentially constant, i.e., the channel network will advect along with the parcel of crust. This initial pattern could have been established by a combination of deterministic submarine processes [see *Orange et al.*, 1994] and random perturbations that together establish an initial surface across which the terrestrial streams first flow and by lithologic contrasts (e.g., the contact between Ben Lomond granite and sur-

rounding Tertiary sediments) toward which the initial stream pattern rapidly slips. In the model described here, the present stream pattern is assumed to record faithfully the initial channel pattern, which is "lightly etched" into the uplifted mass as it emerges from the sea. I then pose physically based models for the response of this channel system and the adjoining hillslopes to tectonically driven uplift.

Hillslopes

Much of the range core is presently dominated by landsliding on the hillslopes and associated debris flows in the channels, in contrast to the diffusion-dominated slopes and incised channels in the marine terraced fringe of the Santa Cruz Mountains discussed by *Rosenbloom and Anderson* [1994]. The landscape evolves under the influence of these discrete geomorphic events driven in turn by weather events [e.g., *Dunne*, 1991]. The problem is stochastic in both time and space, reflecting both the statistics of weather and the spatial variation of both the microclimate and the geologic resistance to landsliding that together make the landscape more, or less, susceptible to failure during a particular storm.

I adopt a strategy that recognizes the gross spatial variation, yet time averages the effects of discrete events in accord with the long timescales involved in mountain evolution. Below, I argue that the hillslope processes can be treated as diffusive in low-lying terrain in which the erosion rates of channels is low and as being driven by landsliding in terrain characterized by high stream incision rates. I also show both that one may scale the steady state local relief in the landscape if the local channel incision rates are known and that the hillslope response times are everywhere much shorter than the channel response times, validating the assumption of steady state local relief. This prompts a model strategy in which the field of channel elevations is explicitly calculated at each time step, from which the field of local relief is easily derived. Hillslopes are neither resolved in the landscape nor is any transience in the hillslope system allowed. The sum of the channel elevation and the local relief is then the maximum elevation of the grid element.

Diffusion

Diffusion of the landscape results from conservation of mass and a transport law that linearly relates mass flux to local slope. Conservation of mass results in the erosion equation

$$\frac{\partial z}{\partial t} = -\frac{1}{\rho_b} \nabla Q \quad (7)$$

where Q is the "specific mass discharge" of sediment on the hillslope, or discharge of mass per unit width of slope [=] M/LT , and ρ_b is the bulk density of the mobile regolith. When this discharge is proportional to the local slope, i.e., when

$$Q = -k \nabla z \quad (8)$$

with k a transport coefficient reflecting the efficiency of the geomorphic process, the erosion equation becomes the diffusion equation

$$\frac{\partial z}{\partial t} = \kappa \nabla^2 z, \quad (9)$$

where $\kappa = k/\rho_b$ is the diffusion coefficient. The transport coefficient and hence the diffusivity will depend upon the

intensity of the process, and can be due to either discrete processes such as tree throw and rodent burrowing, or to continuous processes such as soil creep.

The geometry of the hillslope will be determined by this diffusivity and by the incision rates of the adjacent streams that constitute the lower boundary conditions for the slopes. In the simplest case of a steady state ridge bounded by incising streams, the resulting hillslope profile is parabolic:

$$z = \frac{\dot{e}(L^2 - x^2)}{2\kappa}, \quad (10)$$

where L is the horizontal length of the hillslope, $x=0$ defines the hillcrest, and \dot{e} is the erosion rate of the bounding streams. The local relief, the maximum elevation difference between stream and hillslope, is then

$$R = \frac{\dot{e}L^2}{2\kappa}. \quad (11)$$

In turn, the maximum slope angle will be immediately adjacent to the stream, at $x=L$:

$$\left| \frac{\partial z}{\partial x} \right|_{\max} = \frac{\dot{e}L}{\kappa}. \quad (12)$$

The approach to this steady state under constant incision of channels on either side of the emerging ridge is analogous to the transient thermal problem involving declining temperatures on the edges of a slab with initially uniform temperature [see *Carslaw and Jaeger*, 1986]. Figure 8 shows their solution, converted to the evolution of a ridge line under the above conditions. Importantly, the timescale for the approach to steady state in this diffusive problem is well approximated by $\tau = L^2/\kappa$.

Landsliding

We cannot treat the entire landscape as being diffusive in this simple sense. First, as argued by *Anderson and Humphrey* [1989] and *Rosenbloom and Anderson* [1994], the details of hillslope profiles etched into initially bedrock terrain requires incorporation of weathering processes to produce transportable particles. Second, landslides will occur when a portion of the landscape reaches some failure criterion dependent strongly upon slope angle and importantly upon the local groundwater head gradients on the slope [e.g., *Iverson and Major*, 1986; *Reid and Iverson*, 1992; *Iverson and Reid*, 1992]. Weathering rates limit the rate at which a hillslope will be lowered; if these are smaller than the local incision rate of the stream, no steady state hillslope can be attained with diffusion alone. Rather, the hillslope will continue to steepen, becoming increasingly susceptible to failure by mass wasting. In the center of the range where incision rates of streams are expected to be greatest, we must therefore account for the dominance of landsliding in setting the shapes and scales of the hill slopes.

Landslides may most straightforwardly be incorporated in large landscape evolution models by modifying the flux law $Q(S)$ to accommodate a threshold process. The argument is similar to one made earlier to account for the angle of repose in hillslope evolution models [*Anderson and Humphrey*, 1989]. Hillslopes are characteristically very straight in the mountains, with slight convexity near the base in places (Figure 3). This reflects the operation of discrete failures over long times that efficiently transport mass to the bedrock channel, which then transports the debris from the system. The efficiency of this hillslope process is determined by the typical size and recurrence times of failures.

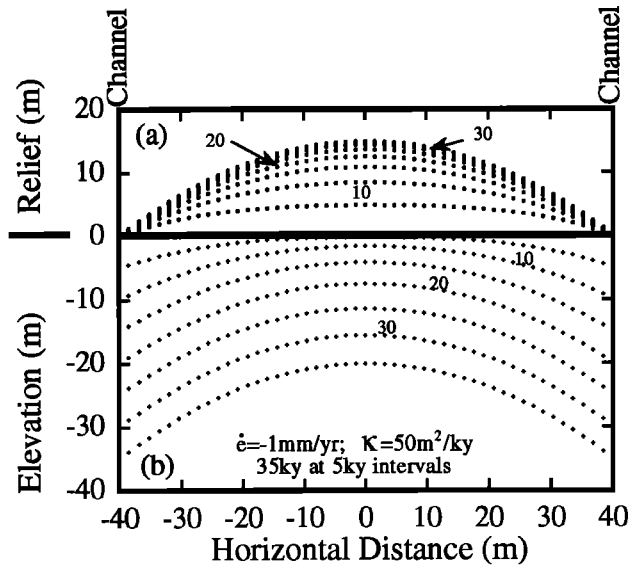


Figure 8. Evolution of an interfluvial profile under the influence of 1 mm/yr incising channels at 40 m from the ridge crest, and diffusive hillslope processes with diffusivity $\kappa = 50 \text{ m}^2/\text{yr}$. In the lower half of the diagram the hillslope profile is shown at 5-kyr intervals (labels every 10 kyr), beginning with an originally flat surface. The profile appears to have attained a steady state form by the end of the calculation. The top portion of the diagram shows this more clearly. Here the profiles are shown with respect to the instantaneous elevation of the channel and therefore allow more exacting comparison of form. The steady state form has indeed been attained by roughly 30 kyr (labels correspond again to times in thousands of years). The steady state relief is approximately 15 m, in accord with the expected relief in purely diffusive systems driven by incision at the boundaries (see text) and is attained in a timescale of roughly L^2/κ .

Given that these failures can involve the entire soil column and sometimes substantial quantities of bedrock, the efficiency of landsliding can be very much higher than the diffusive processes that operate necessarily only on surficial material. An effective diffusivity may be constructed from the typical path lengths for the landslides L and the recurrence times τ through L^2/τ . The probability of a failure increases with the approach of some local part of the slope toward a critical angle. These statements may be cast formally as a modification to the pure diffusion transport rule such that

$$Q = -k_d S - k_{ls} S_c \left[\exp\left(-\frac{S_c - S}{S_*}\right) \right], \quad (13)$$

where S is the local slope, S_c is the critical slope, S_* is a slope scale determining how close the slope must be to the threshold slope before the probability of failure is greatly increased, k_d is the normal diffusivity, and k_{ls} is the maximum effective diffusivity resulting from landslides. Note that at $S=S_c$, $Q = (k_d + k_{ls}) S_c$. A relative enhancement of the transport process by landsliding, $\gamma = k_{ls}/k_d$, may be defined such that when $\gamma=1$, landsliding and diffusion contribute equally to the mass transport at the threshold angle S_c . The coefficient S_* reflects the expected spatial variation in the failure potential within the landscape due to variations in (1) lithology, structure and root strength setting the resisting forces, (2) the groundwater field, and (3) the

intensity of groundshaking associated with seismic events. I expect that the scale of S_* will determine how closely the steady state hillslope will approach the threshold slope (Figure 9).

The maximum possible hillslope relief in this landsliding-dominated landscape is $R = L \tan(S_c)$. Actual values will be

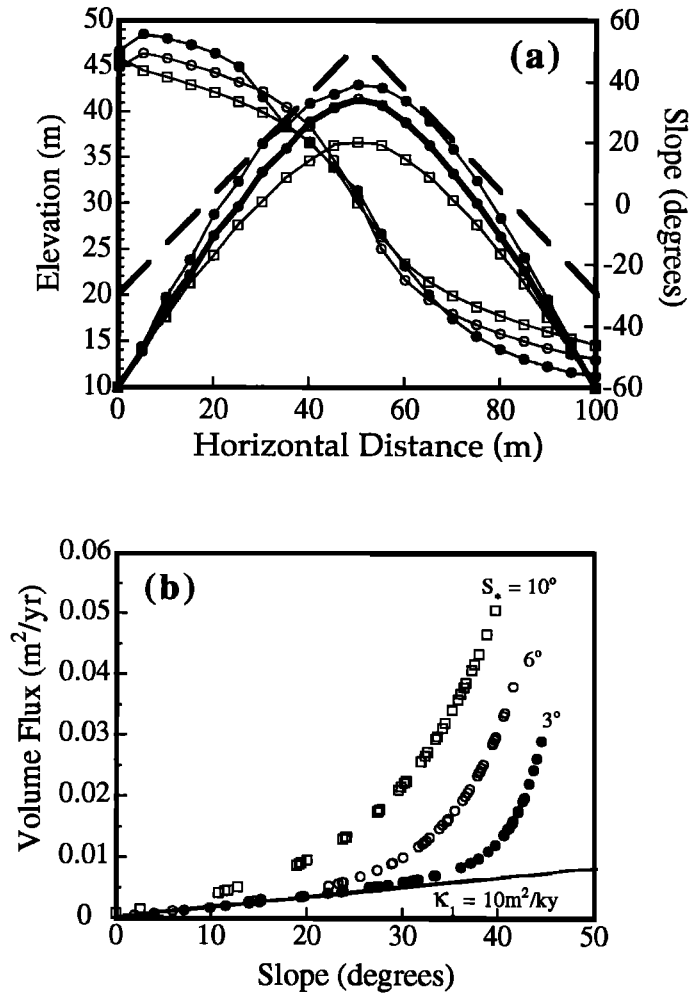


Figure 9. Hillslope evolution due to a linear flux law modified at high slopes to account for more efficient transport by landsliding. (a) Cross section of the topography calculated from an initial condition of straight slopes, and boundary conditions supplied by equal channel incision rates at the two sides of the calculation space. Also shown are the slope angles, the derivative of the topography, with corresponding symbols. The flux laws used to drive sediment downslope are as shown in Figure 9b, the three cases corresponding to the three flux laws, with matching symbols. (b) Transport law in which lane width volume flux exponentially increases above that due to diffusive processes (κ_1) as a threshold slope S_c (here 50°) is approached, the characteristic slope scale for the exponential approach being S_* (here 3° , 6° , and 10°). The resulting steady state forms have nearly uniform straight slopes near the base, and convex crests near which the low angle slopes allow diffusive processes to dominate. (For comparison, note that parabolic purely diffusive profiles (see Figure 8) would display a linear dependence of gradient on position, i.e., a uniform curvature.) The basal slopes are controlled by the sensitivity of the flux law as it approaches the critical angle, and are roughly $S_c S_*$. Steady state relief is therefore well approximated by $R = L \tan(S_c S_*)$.

considerably lower, given rounding of crests due to diffusion, and earlier lower-angle failures associated with the scale S_* . Simulations such as those shown in Figure 9 show that a better approximation might be $R=L \tan(S_c - S_*)$.

We may now assess under what conditions the relief will be determined by diffusive processes versus landsliding processes. Diffusive processes will no longer dominate when the maximum slope begins to approach the landsliding threshold, i.e., when $S_{\max} > S_c - S_*$. Recalling that the maximum slope in a steady state diffusive landscape (with parabolic hills) is $\dot{c}L/\kappa$, we therefore expect that landsliding will set the local relief of the landscape when $\dot{c} > [\kappa(S_c - S_*)]/L$. Otherwise, the local relief will be determined by the diffusive steady state (equation (11)).

Stream Channel Incision

As has been demonstrated by earlier modeling efforts [Koons, 1989], the large-scale topographic evolution of a mountain range cannot be modeled without proper attention to the incision of stream channels into the uplifting rock mass. Koons proceeded by simply draping stream channels within the mountain belt, specifying a characteristic logarithmic shape to the longitudinal profiles of each stream. Here I attempt to incorporate a process-related stream incision rule of the type described in greater detail by Seidl and Dietrich [1992] and as applied to the streams incising the marine terraces of Santa Cruz by Rosenbloom and Anderson [1994]. The stream is assumed to incise at a rate dictated by the local stream power, or the energy lost by a parcel of water per unit time per unit downstream length of channel. This energy goes into heat within the water mass, into the transport of sediment, and into degradation of the bed. The stream power may be cast as the product of the discharge of water (or water discharge) and the slope of the bed:

$$P = \rho g H W \bar{u} \sin(\alpha) = \rho g Q_w S \quad (14)$$

where Q_w is the water discharge, and for small angles the sine of the slope is approximately the tangent of the channel slope S .

In keeping with the large spatial and temporal scales required, I do not incorporate individual storm events from which one might calculate both spatial and temporal patterns of stream power with position in the stream system, a strategy illustrated by Dunne [1991] on hillslopes. Earlier workers [e.g., Howard and Kerby, 1983; Seidl and Dietrich, 1992; Howard et al., 1992] have proposed the use of the drainage area as a surrogate for the water discharge in such events. This approach is followed by Rosenbloom and Anderson [1994], although in the channel reaches they addressed, the additional assumption that the drainage area was effectively uniform was justified. Here, I slightly refine this approach in two ways. I take the product of the drainage area and the average rainfall above a particular point on the channel stand as the surrogate for the local water discharge. The incision rule then becomes

$$\frac{\partial z}{\partial t} = -c A \bar{R} S \quad (15)$$

where A is the basin area above the channel point, \bar{R} is the average precipitation rate in that area, and c is an empirically determined constant that reflects the proportion of the stream power expended in incision of the channel. If, on the other hand, one assumes that rainfall is constant within the drainage basin, the rainfall term is subsumed in the coefficient c and we return to the simplest slope-area product formulation.

In addition, I attempt to account for the expected change in process in the upper reaches of the drainage system, where debris

flow scour of the channels increases the dependence of the incision rate on the local slope of the channel [Seidl and Dietrich, 1992]. The incision rule is the same as that in equation (15) except that the dependence on S is nonlinear. I take the dependence to go as S^2 , knowing that this only crudely accounts for this poorly constrained process.

Figure 10 shows the evolution of a longitudinal cross section of a channel with initially straight slope, when acted upon by the simple slope area product rule. Here the area of the drainage basin, A , is assumed to increase with distance down the channel, x , as a power law $A=x^{5/3}$; this is meant to approximate typical basin geometry. Base level is assumed to remain constant and is imposed by forcing the channel slope to vanish at base level. I define a threshold distance from the drainage divide, x^* , above which channelization is not allowed. The channel incises most deeply into the central region of the basin; the low slopes near the mouth of the channel inhibit erosion, while the low drainage area inhibits incision in the upper reaches.

The Single Drainage Basin: An Interior Model Approach

One may take any of several possible approaches to the problem of how to treat the finer scale topography within a coarse model grid. An interior model could be constructed that displays the dynamic response to changes in the conditions imposed upon a grid cell by the surrounding channel and drainage divide boundaries. This would allow the transient responses of the hillslopes and the channel to be explicitly linked within the system. If the problem scale demands such resolution, this would be appropriate and in certain instances can be made quite compact. Below I illustrate such a solution to the single first-

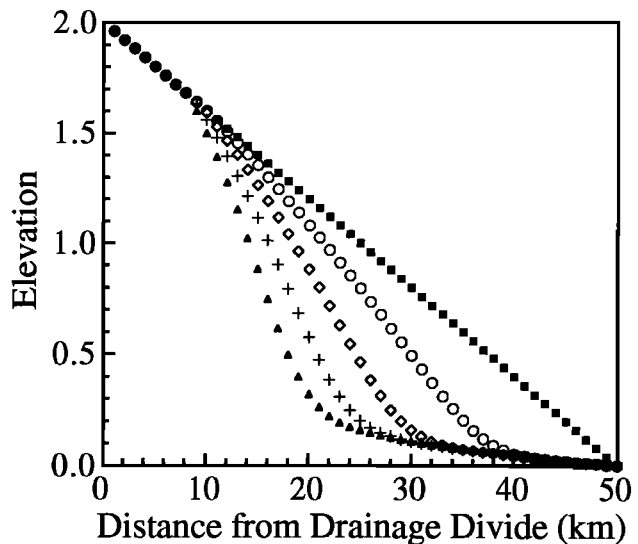


Figure 10. Bedrock channel incision history driven by stream power or area-slope product rule. Initial condition of a straight profile with gradient of 4.0×10^{-4} , and four subsequent times in the calculation are shown. Drainage area is assumed to increase as distance downstream to the $5/3$ power. The channel head is arbitrarily taken to be 10 km from divide. The zero-slope boundary condition at the mouth of the system dictates the low slopes of the lower reaches. No area at the channel head requires incision to vanish there as well (no headward retreat of the channel head is allowed). The channel profile therefore droops into bedrock with maximum erosion where the slope-area product is greatest, resulting in headward migration of the region of greatest concavity.

order basin response and use it to assess the relative timescales of channels and hillslopes in the larger-scale problem. Ultimately, I determine that the timescales of hillslope response are far shorter than the response of the channel system, motivating use of the assumption of steady state relief.

Consider a single first-order channel within a very simplified rectangular drainage basin of width $2W$, containing a channel of length L_c . The distance from the drainage divide to the tip of the channel is x^* . The dependence of drainage area on position within the channel is linear: $A = A_0 + 2(L_c - x)W$, x being the upstream distance from the tributary junction at the base of the drainage, W being the hillslope length and A_0 being the drainage area contributing to the channel head (representing the area in the threshold slope-area product necessary to generate a channel as argued by *Montgomery and Dietrich* [1990] and *Dietrich et al.* [1992, 1993]). The processes are taken to be diffusive on the hillslopes, and to be controlled by the stream power rule described above within the channel. The system is perturbed at time $t = 0$ by a simple base level drop dz at the channel junction, for instance by the passage of a knickpoint in the trunk stream [Seidl and Dietrich, 1992]. The integrated response is measured by the discharge of sediment from the system, which yields a history of mean denudation rate when divided by the basin area. Formally, the response of the system in terms of sediment discharge is a convolution integral

$$Q = 2 \, dx \int_0^{L_c} q(t-\tau) \, dt \quad (16)$$

where $q [=] M L^{-1} T^{-1}$ represents the hillslope response function after rejuvenation and τ is the time since passage of the knickpoint: $\tau = x/(u(x))$. Here the average speed of the knickpoint up to this position in the channel $\langle u \rangle$ is calculated from the mean of all local speeds of the knickpoint $u = c(A_0 + 2(L_c - x)W)$ from $x=0$ to the point of concern. The hillslope response function may be solved by appeal to the analogous heat flow problem of a finite slab (ridge) of thickness $2W$, initial conditions of a parabolic steady state thermal (topographic) profile and step changes in the temperature (elevation) boundary conditions at each edge by ΔT (Δz) at $t=0$ [see *Carslaw and Jaeger*, 1986]. The resulting discharge or denudation history is shown in Figure 11.

Physically, as the knickpoint created by the base level drop at the tributary junction migrates headward, it rejuvenates the adjacent slopes, which begin to deliver more material to the channel, thence out of the system. The headward march of the channel convexity slows as the drainage area above it declines. Once this convexity reaches the channel tip, the channel has fully responded to the perturbation, and the remaining sediment flux history is due solely to the response of those hillslopes most recently rejuvenated.

Importantly, two timescales emerge in the problem, one associated with the hillslope response, the other with the channel response. As determined above, the hillslope response time is scaled by L^2/κ . The channel response time is scaled by the channel length and the average migration velocity of the knickpoint, which results in

$$\tau_{ch} = -\frac{1}{2cW} \ln \left(\frac{A_0}{A_{total}} \right), \quad (17)$$

where A_{total} is the total drainage basin area. When the hillslope response time is very short compared to the channel response time, the hillslopes will essentially always be in equilibrium with the local channel incision rate.

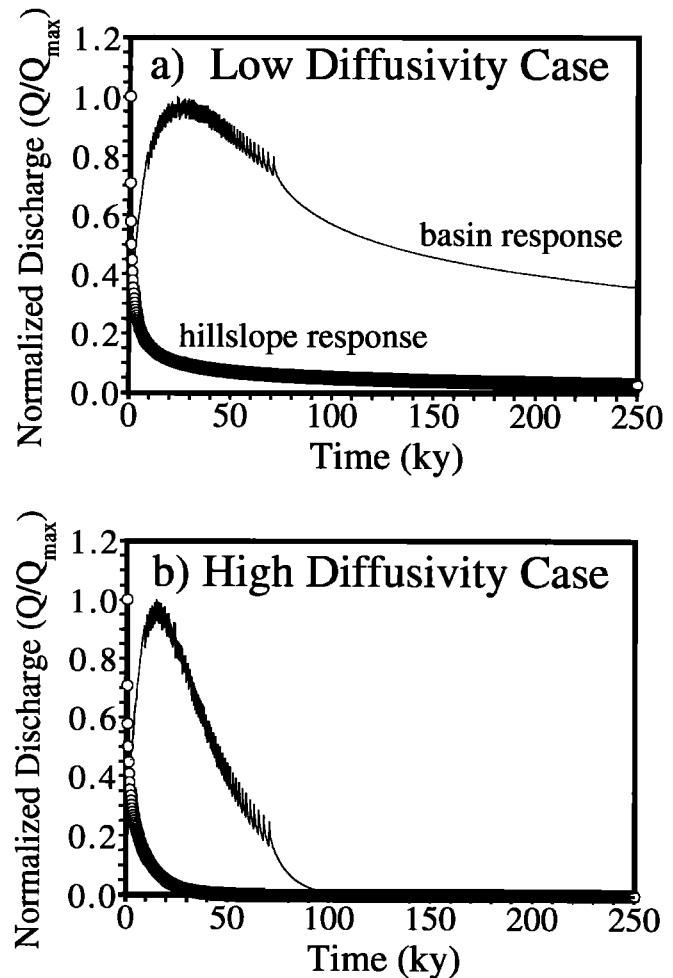


Figure 11. Drainage system response to a 2-m base level drop at time=0. Simplified drainage basin has 100 m hillslopes on either side of a 1-km-long channel extending to within 100 m of the drainage divide. Hillslope processes are taken to be diffusive, (a) $40 \text{ m}^2/\text{kyr}$ and (b) $400 \text{ m}^2/\text{kyr}$. Channel incision proceeds by propagation of a knickpoint at a speed dictated by the local drainage area above the convexity and the channel incision constant, $c = 2 \times 10^{-7} \text{ m}^{-1} \text{ yr}^{-1}$. Smooth declining line is the hillslope response curve, $q(t)$, for a single hillslope perturbed at its base at time=0 by a channel incision event, such as the passage of a knickpoint past the base. Timescale for response goes inversely as the diffusivity. Drainage system response is displayed as history of sediment discharge from the basin, normalized against the maximum discharge. Discharge smoothly increases as knickpoint migrates headward, turning on progressively more hillslopes. Propagation velocity of the knickpoint slows as it loses drainage area toward the head of the channel. Sawteeth in the plot reflect discretization of the channel length; at low knickpoint speeds, significant hillslope response occurs before the next increment of hillslope is perturbed. The channel head has been reached at 70 kyr. Thereafter the discharge history is entirely dictated by the flux of sediment from the most recently rejuvenated hillslopes. Note the system response time is dictated in Figure 11a) by the hillslope response time and in Figure 11b) by the channel response time.

I argue that in the landslide-dominated majority of the Santa Cruz Mountains the high effective diffusivity associated with landslides dictates that this is the case, and one may proceed with an even simpler strategy that ignores the hillslopes' transience.

On the other hand, the marine terraced portion of the landscape is clearly in a state of transience; the younger broad flat terrace interfluvies have not yet responded to the downcutting of channels through the terrace sequence. In the terraced fringe, the effective diffusivities are low ($10 \text{ m}^2/\text{kyr}$) and the hillslope timescales are therefore of the order of several hundred thousand years. The topographic details of interest in this smaller scale landscape demand a much more finely gridded model [Rosenbloom and Anderson, 1994] than the one employed herein.

Summary of Geomorphic Model Strategy

The above discussion of the geomorphic processes leads to several key assumptions embedded in the model. I assume that relative to the channels, the hillslopes come quickly to a steady state form. This justifies the imposition of steady state local relief along a channel reach (i.e., within a grid cell) without carrying out the time-dependent calculation illustrated above. I emphasize that hillslopes are not resolved in the model landscape. Rather, a cell has two altitudes, one corresponding to the channel elevation, and another corresponding to the hillcrests (channel elevation plus relief).

The local rate of incision of the stream channel into bedrock, calculated at each time step according to the slope-area product, sets the local relief. For the low incision rates associated with the stream mouths, the steady state relief is calculated assuming that diffusion dominates the hillslopes. Above some point on the channel, the incision rates become high enough to cause slopes adjacent to the channel to fail as landslides; here a different local relief is fixed by the slope angle and the hillslope length.

The geomorphic rules are therefore confined to that for stream incision and a calculation of local relief that is process dependent. Only the largest channel in any cell is assessed, the smaller tributaries responding on much shorter timescales. In addition, the known shapes of the steady state hillslopes allow simple calculation of the mean elevation in a pixel: $\langle z \rangle = z_{ch} + 0.667R$ in the case of the parabolic diffusive ridges and $\langle z \rangle = z_{ch} + 0.5R$ in the landsliding-dominated ridges, where z_{ch} is the local channel elevation and R is the local relief.

Model Setup

The model space representing the present extent of the Santa Cruz Mountains is subdivided into $4 \times 4 \text{ km}$ pixels. The SAF is the boundary between the two model halves. Note that the fault is straight, as dictated by the fact that the grid cannot deform. The relative slip rate across the fault is prescribed as U_{rel} . That landscape to the NE of the fault all migrates to the SE at the same rate, U_e , while that on the SW of the fault all migrates at a prescribed rate, U_w , to the NW, the two speeds related through $U_{rel} = U_w + U_e$. No deformation of the grid is allowed, only translation parallel to the SAF. The uplift pattern is fixed in space and is centered at (0,0) (Figure 7); the speeds U_w and U_e therefore represent speeds relative to this uplift pattern. The uplift pattern is specified, and the elastic constants and density contrast parameters controlling the deflection are as listed in Table 1, which lists all model parameters required.

Rather than determining by scrutiny of maps the drainage area above each node in the model, as needed in the stream incision algorithm, I have inferred drainage area from the Shreve magnitude, M_s , of the stream at each node (Figure 12). The Shreve magnitude represents the sum of the upstream first-order drainages at any point on the channel [Shreve, 1966]. For the Santa Cruz Mountains, a roughly linear relationship exists

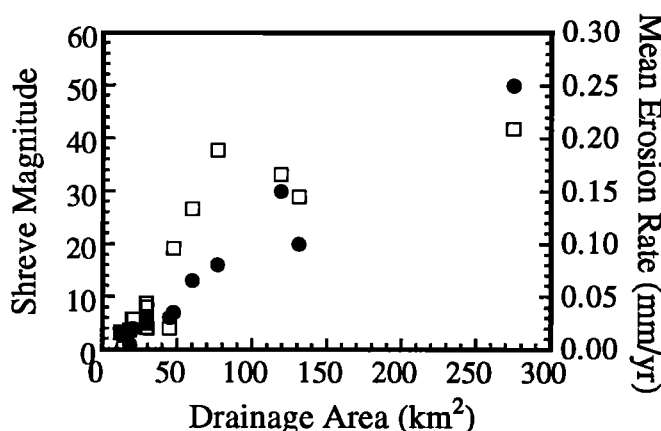


Figure 12. Shreve magnitude [Shreve, 1966] (dots) and erosion rate (squares) as functions of drainage area for 13 coastal Santa Cruz streams. Note that Shreve magnitude (number of first-order tributaries in the basin) is a good estimator of the drainage area, the inferred mean first-order basin area being roughly 5 km^2 . Erosion rates calculated from sediment fluxes [Best and Griggs, 1991] increase with drainage area, primarily because only the larger streams access the high rainfall center of the range. Basin average erosion rates are probably of the order of 0.2 mm/yr for much of the mountains.

between the drainage area of the major streams (tabulated by Best and Griggs [1991]) and the Shreve magnitude (as measured on 1:100,000 maps), implying that the mean size of a first-order drainage on such maps, A_1 , is a constant, about 5 km^2 . The drainage area at each node is therefore taken to be $A = M_s A_1$. I note that this approach to obtaining drainage area is crude, that closer map scrutiny would certainly yield a more detailed picture, and that use of maps of a different scale would undoubtedly yield a different measure of the area corresponding to first-order basins. However, given the coarse nature of the grid on which the model is calculated (with 16 km^2 pixels), the effort involved is not commensurate with the goal of efficient modeling. While the drainage area above a channel point will not change with time, in accord with the assumption that the stream pattern is the most slowly changing aspect of the landscape, the mean precipitation above a point could be allowed to change with growing orographic effects and with global climate swings. This has not been instituted in the present study.

The initial topography is taken to be flat, with all channel elevations and relief set to zero. Channels are therefore only "lightly etched"; the drainage area associated with each node is specified as described above, and the direction of flow between adjacent pixels is fixed (in general, down the highest gradient in Shreve magnitude). The geomorphic processes and rates are specified through the assignment of a hillslope diffusivity κ , a channel incision parameter β , and a critical slope S_c , above which landsliding is expected to dominate.

The model time step is chosen to be small enough to ensure stability of the channel profiles. Insufficient parsing of time results in overdeepening of channels and a reversal of gradients in places experiencing high incision rates. This is typically 40 kyr . The model is allowed to run for times of either 4 or 8–10 m.y. The shorter interval corresponds to the time in which the plate margin has been in slight compression [e.g., Page and Engbreton, 1984]. The longer time represents a conservative estimate of the time since the passage of the triple junction [e.g.,

Irwin, 1990]. The deflection field is calculated less frequently, every five time steps.

Results

I monitor the development of several fields within the model space. The topographic fields are represented by (1) channel elevation, (2) relief, and (3) mean elevation. The flexural deflection field associated with the mean elevations is recorded, allowing the possibility of predicting gravity anomalies. I calculate the rock uplift pattern by retaining the topographic field that would result in the complete absence of geomorphic modification of the uplifted mass. This allows the calculation of the exhumation field, the difference between the rock uplift pattern and the surface topography. In addition, we may track the elevation, exhumation, and deflection histories of particular parcels of crust and of statistical properties of the landscape such as the hypsometric curve and the mean elevation. The results are therefore testable against a number of data sets; only a few of these possible comparisons are shown here. The most areally extensive and most easily accessible data set is the topography itself. Others include the gravity field, the distribution of relief, the elevation of bench marks, the dip of originally flat surfaces, and exhumation rates at points as deduced from fission track analyses.

The resulting topography (mean elevations in each 4x4 km pixel) is shown in Figure 13 along with the actual topography. Many of the gross features of the Santa Cruz Mountains are

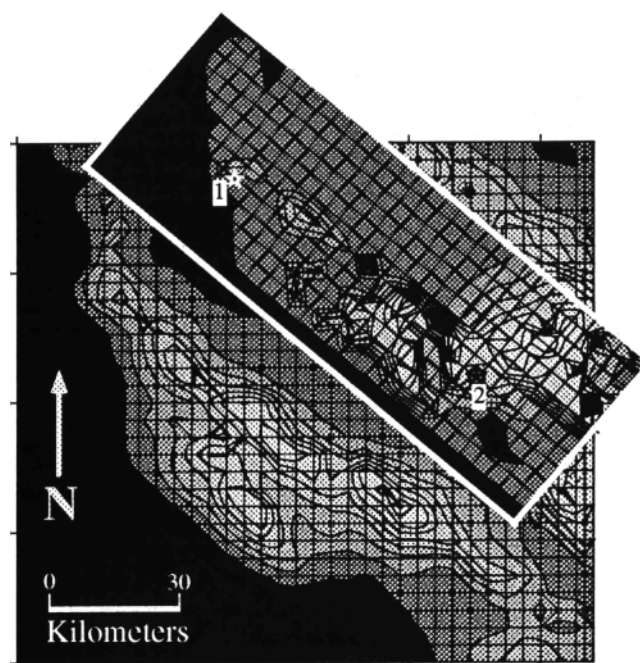


Figure 13. Overlay of calculated over real topography, both with 100-m contours, for the model input parameters listed in Table 1. Maximum elevations are approximately correct. The ranges have the correct dimensions, both in length and in maximum altitude. The major streams on the west coast, the San Lorenzo River and Pescadero Creek, are shown wrapping behind the prominent Ben Lomond Mountain massif. This massif has not been attacked significantly on the coastal side, which sports only low order drainage basins. See text for discussion.

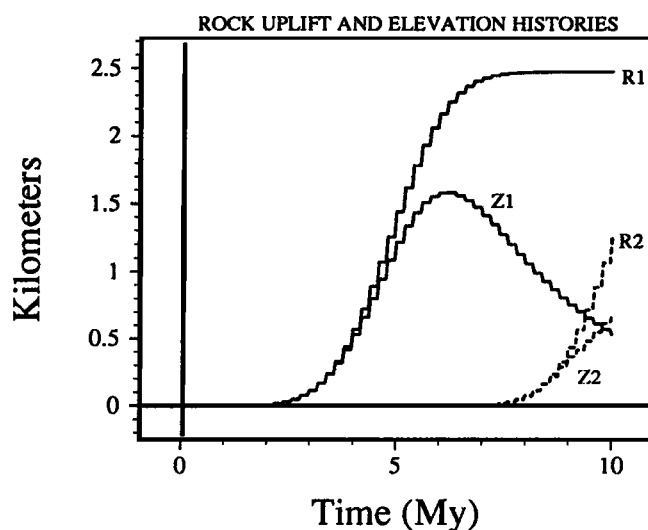


Figure 14. Rock uplift (R) and elevation histories (Z) for two points (1 and 2) within the calculation space. Point 1 is found at the end of the calculation at (64,4), while point 2 is (0,4) (see labels in Figure 13). Slip rate with respect to the bend, $U_{\text{west}} = 10 \text{ km/m.y.}$ Uplift rate maximum is 1 km/m.y. in the uplift center. Delay between uplift of points 1 and 2 corresponds to the different times they encounter the uplift pattern. Divergence of elevation of a point from the rock uplift reflects geomorphic erosion, which in turn is dependent upon the local channel system. Point 1 is adjacent to the uplift maximum at roughly 5 m.y., resulting in its highest rock uplift rate then. Its elevation maximum is attained about 1 m.y. later, and it decays monotonically thereafter as geomorphic erosion processes outstrip rock uplift. Maximum elevations in the range should therefore be about 10 km downslip from the uplift rate maximum, and the maxima of the northern and southern ranges should be shifted from one another by two times this, or 20 km. This is approximately the case (see Figures 1 and 13).

reproduced. The general decay of the range downslip from the edges of the uplift pattern is clear. The major stream valleys are now etched deeply into the topography, the most notable of these being the San Lorenzo River separating the Ben Lomond massif from the crest of the northern range. The maximum elevations of the range crest and the principal subsummits of the northern range are roughly in their proper places and are roughly correct in their altitudes.

The rock uplift and elevation histories of two parcels of crust (labelled in Figure 13) are shown in Figure 14. Both points are 4 km from the SAF on the Pacific Plate. At the end of the calculation, the first point is 64 km NE of the uplift maximum, while the second has just reached the uplift maximum. The rock uplift histories reflect the integrated uplift rate along the path of the parcel of crust. The traces are therefore parallel but offset by a time corresponding to their horizontal separation: $t = (x_1 - x_2)/U_{\text{west}}$. The elevation histories diverge from the rock uplift histories once the geomorphic processes have become more efficient due to enhanced channel gradients. Eventually, the erosion rates become greater than the uplift rates, and the topography decays. Maximum elevations in the model therefore correspond to the positions at which uplift and erosion are equal. Inspection of Figure 14 reveals that there is roughly 1 m.y.

between passage of the crust past the uplift center and the achievement of this balance, a time corresponding to 10 km of slip with respect to the bend (assuming 50% displacement on each side of the fault and 20 km/m.y. relative slip). This should happen on both sides of the fault. The topographic maxima of northern and southern ranges therefore ought to be separated by approximately 20 km.

The rock uplift pattern and the exhumation pattern are shown in Figure 15 at the end of a 10 m.y. model run. Rock uplift results from uplift within the bend region and translation of the uplifted mass with respect to the bend. The pattern demonstrates that the entire length of both halves of the range may be created in the time available, given the long-term slip rate on the San Andreas Fault. The amplitude of the pattern is dictated by the time a parcel of crust spends within the uplift pattern. Although the relative slip is fixed by geological constraints, the relative amplitude of the rock uplift on the two sides of the fault may be adjusted by placing more of the slip with respect to the uplift pattern on one or the other side of the fault. For example, in

Figure 16, 75% of the slip is allowed to take place on the west of the fault, resulting in significantly more uplift of rock on the east side as it spends more time traversing the uplift pattern.

The exhumation pattern is also depicted in Figure 15. That this so closely mimics the rock uplift pattern shown in the bottom panel implies that the majority of the rock mass lifted above zero altitude in the bend region has been removed by subsequent geomorphic processes. Given the high efficiency of the geomorphic processes, it is the rock uplift magnitude more than the geomorphic erosion rate pattern that appears to be reflected in the exhumation pattern. Such patterns are commonly documented through the use of fission track analyses [see *Burgmann et al.*, this issue]. Whether the magnitude of the exhumation is sufficient to have been recorded in fission tracks depends upon whether the amplitude of the rock uplift is sufficient to have lifted the rock parcel through a great enough range of temperatures.

The deflection field at the end of a model run is shown in an oblique view in Figure 16. Note the small amplitude of the pattern, of order 10-20 m, which is typical of all other model

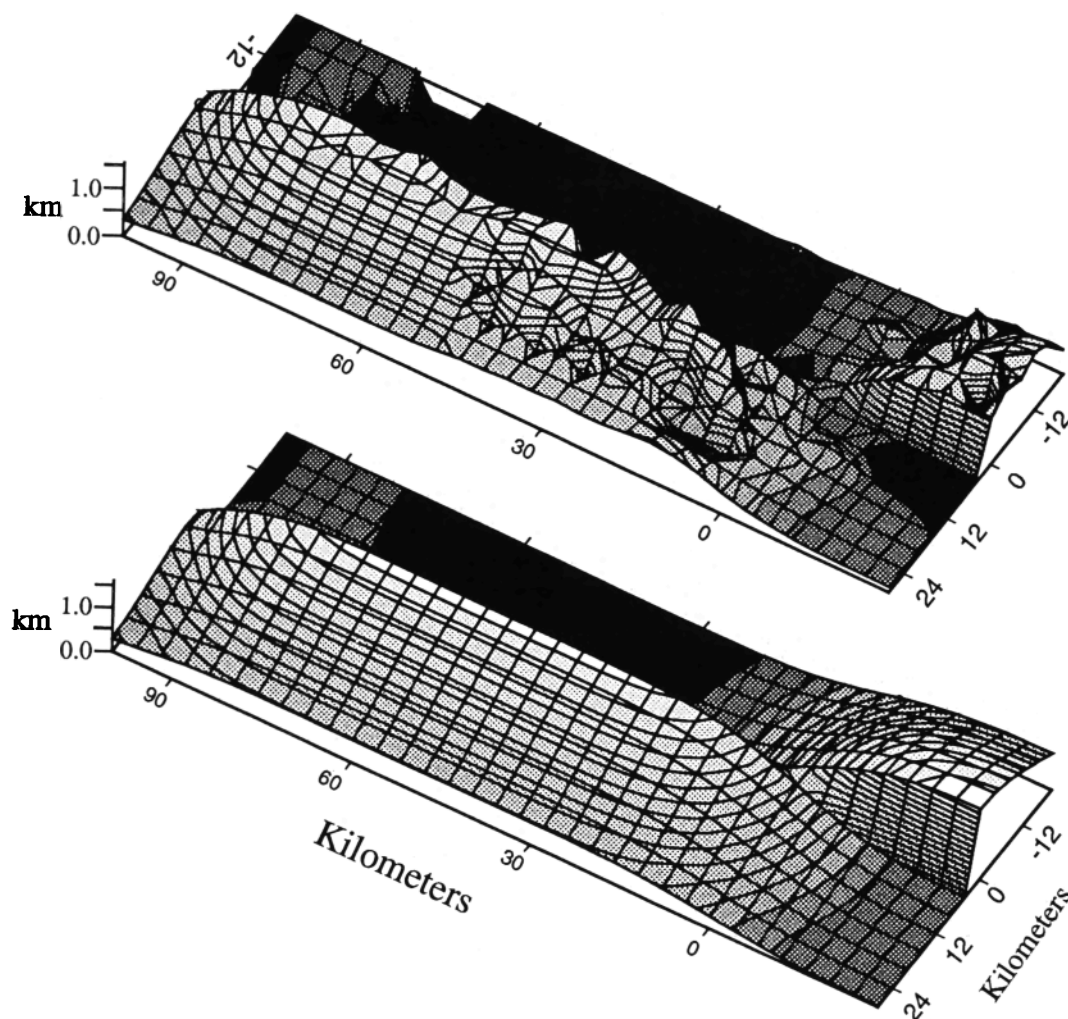


Figure 15. Aerial view from SW of an example of a calculated exhumation pattern, with 200-m contours. That the exhumation pattern so closely reflects the rock uplift pattern (shown in bottom of diagram for comparison) implies the geomorphic processes are efficient enough to remove almost all mass lifted past the original sea level datum. Maximum possible exhumation in this case should be of the order of 2 km for the chosen uplift pattern and the chosen partitioning of slip relative to the bend. This maximum exhumation ought to be achieved well downslip from the uplift source, where the topography has been subjected most extensively to geomorphic processes. This is where the exhumation and rock uplift patterns match most closely.

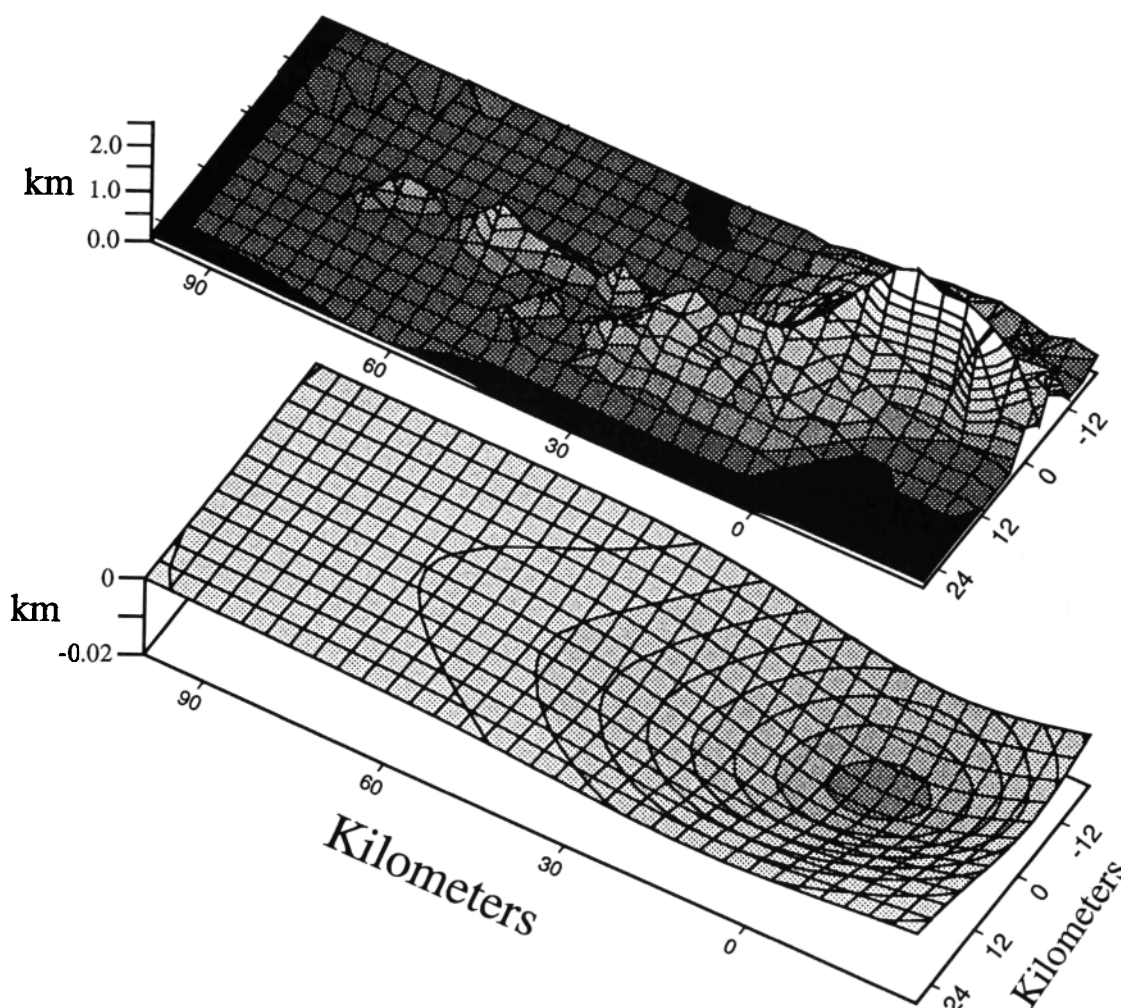


Figure 16. Oblique view from SW of topography (100-m contours) and resulting crustal deflection (5-m contours) for case in which the slip with respect to the bend is chosen to be asymmetric, the west side slipping at 15 km/m.y., the east at 5 km/m.y. (retaining relative slip of 20 km/m.y.). Note the high southern Santa Cruz Mountains crest relative to that of the northern range, and the retention of significant topography well down-slip to the NW on the west side, due to its rapid transit. The largest crustal deflection is shown beneath the most extensive mountains and has decayed to near zero beneath the most downslip portion of the northern range.

runs. The majority of the topographic load is being supported by the flexural strength of the elastic portion of the lithosphere, even for the chosen relatively small elastic thickness of 5 km. Deflection histories of the same two points depicted in Figure 14 are shown in Figure 17. Note that the deflection grows to a maximum, associated with maximum growth of the range crest overhead and subsequently decays as the load is diminished through erosion. Thus both flexural subsidence and uplift has been accomplished, although they are of small amplitude in this particular range. Importantly, the timing of the rebound is delayed from that of the decay of topography at a point. The flexural rigidity of the crust causes rebound to be a regional effect. A parcel of crust may not rebound until the mean load, averaged over a rather long distance determined by the flexural parameter, is reduced. In this case, it took roughly 1 m.y. beyond the time at which the elevation of the parcel began to decline for rebound to be enacted.

Typical model results not shown also show that the maximum elevation reaches a steady state of approximately 1 km within about 4 m.y., while the exhumation continues to grow for another 2 m.y. before reaching a steady value of more than 2 km.

Reminiscent of the histories of individual point elevations (Figure 14), the maximum elevation grows more rapidly than does the maximum exhumation. This may be interpreted as signifying that the geomorphic processes driven by the lower gradients early in the calculation time are insufficient to drive significant geomorphic decay. The topography at this time is determined largely by the rock uplift pattern. Subsequently, the growing topographic gradients force greater incision rates, and exhumation rates eventually outstrip rock uplift rates. The time to reach maximum topography corresponds to the time necessary to translate a parcel of crust through the uplift region to the point at which erosion equals uplift. The attainment of statistically steady topography, however, is roughly the time it takes to reach the maximum exhumation, by which time the parcel of uplifted crust has been beveled by erosion. Given that the simulation lasts more than this 6 m.y., the topography would look statistically the same from 6 m.y. through 8 m.y., the end of this particular run. The hypsometry of the range, a representative statistical description of the range shape, is shown in Figure 18 at four different times within the calculation. One may see that the range has reached a statistical steady state by roughly 6 m.y.

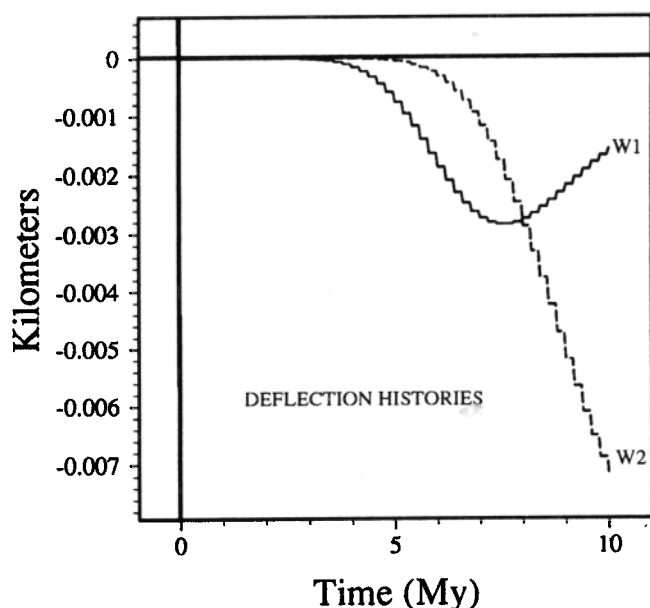


Figure 17. History of deflection, W , of two parcels of crust within the northern range. Point 1, solid line labeled W1, is presently near Montara mountain in the northern San Francisco peninsula, while point 2, labeled W2, is a similar distance from the SAF but is presently adjacent to the uplift source (see Figure 13 for locations). These correspond to the points for which rock uplift and elevation histories were recorded in Figure 14. Calculated deflection magnitudes are small, reflecting the small scale of the mountain range (mean elevation about 250 m). Rebound of the northern point is forced by geomorphic decay of the range as it translates away from the uplift region. Rebound is suppressed for about 1 m.y. beyond the time at which the point reaches its maximum elevation (compare Figure 14) due to the regionalization of the load by the flexural rigidity. The flexural parameter implied by the choice of elastic constants is roughly 12 km, meaning loads are significantly felt for about this distance.

Discussion

Discussion of the Santa Cruz Mountains Application

The hypothesis that the Santa Cruz mountains may be explained as a consequence of an uplift source associated with the fault bend, translation of the crust on either side of the fault with respect to the bend, and geomorphic attack of the tectonically produced rock uplift appears to be supported. A reasonable landscape is developed using measurable geomorphic parameters. The diffusivities used are of order tens of square meters per thousand years, in accord with measured values of $11 \text{ m}^2/\text{kyr}$ [Rosenbloom and Anderson, 1994] and $35 \text{ m}^2/\text{kyr}$ [McKean *et al.*, 1993]. The constants controlling the incision rates of channels are not greatly different from those that best fit stream channels crossing the terraced fringe of the landscape [Rosenbloom and Anderson, 1994].

That the model topography approaches the real topography using a stationary uplift pattern associated with the bend in the San Andreas Fault suggests that the bend is a long-lived feature of this portion of the plate boundary. Although I have not explored the full range of possible partitionings of fault slip onto the two sides of the fault, the shorter fault-parallel length of the

southern range might suggest slower translation of the eastern crust with respect to the uplift pattern associated with the bend. The corollary to this is that the southern range should have experienced more rock uplift than the northern range. Given the roughly similar maximum altitudes of the northern (1100 m) and southern (900 m) ranges, the exhumation of rock in the southern range should be greater than that of the northern range. Comparison of measured and model-predicted exhumation fields may therefore provide a test of this statement. Insufficient data currently exist. However, the exhumation rates calculated here are compared with the few data derived from fission track counts and length distributions in apatites sampled from near the southern range crest; time since closure at approximately 100°C is estimated to be 4 Ma [Burgmann *et al.*, this issue]. If the long-term geothermal gradient is assumed to be consistent with present regional gradients of $25^\circ\text{C}/\text{km}$, then these data imply exhumation rates of order $1 \text{ km}/\text{Ma}$ in the southern Santa Cruz Mountains [Burgmann *et al.*, this issue]. That this is approximately the expected mean thickening rate necessary to accommodate conservation of mass in the bend, as assumed in the generation of the model-uplift algorithm, implies that the majority of the crustal thickening has been stripped away by geomorphic processes (i.e., rock uplift rate equals exhumation rate), and that no significant root should exist. On the other hand, the model results from the equi-partitioned slip case do not reproduce rock uplift of the magnitude necessary to allow 4 km of exhumation (maximum exhumation is 2.4 km). In order to reconcile the two, one either needs to call upon another uplift mechanism and hence uplift pattern altogether or to partition less relative slip onto the east side of the SAF (e.g., Figure 16). It is also probable that the actual long-term uplift pattern could differ considerably from that I have used in the calculation, given the inadequacy of a simple symmetric bend to capture the reality of the fault geometry.

Given the small amplitude of the deflection field (Figure 17), it would seem appropriate to ignore the flexural deflection altogether. However, the shape of the subtle moat around the mountains, in particular to the NE of the bend, is worth noting, as the gravity field associated with it may represent a testable feature. Indeed, the measured Bouguer gravity anomaly field [Chapman and Bishop, 1968] displays the most prominent gravity low (-25 mGal) in this southern San Francisco Bay area region, indicating a slight deflection of the density contrast surface at depth. In addition, the low amplitude of the deflection, even for the chosen small elastic thickness of 5 km, implies that the majority of the crustal thickening associated with the fault bend goes into surface rock uplift.

The range is simply insufficient in scale to cause significant flexure. This in turn disallows the interesting erosional feedback occurring in larger mountain ranges, generated by the evolution of relief. Nonetheless, a closer comparison of the measured gravity field with a model-generated gravity field, which could easily be incorporated in the model algorithm, would provide another test of the model.

Discussion of the Model Strategy

Tectonic forcing. The tectonic forcing in the present model is admittedly crude and can be improved through thoughtful application of recently emerging boundary element techniques. Recent geodetic evidence [e.g., Lisowski *et al.*, 1990] points toward very high, short-lived, near-fault vertical motions that call into question the degree to which the uplift field may be estimated using purely elastic models. Nonetheless, over the several hundred thousand years represented by the Santa Cruz

marine terraces, the far-field (>5 km) uplift pattern mimics well the expected uplift from dislocations on individual active fault structures [Valensise and Ward, 1991; Anderson, 1990; Anderson and Menking, 1994], implying that over these time intervals the vertical uplift pattern may be well modeled by boundary-element and other elastic dislocation techniques.

The scale problem. The model diverges from the approaches taken by other researchers, all of whom evolve topography on a gridded landscape. Chase [1992] demonstrates the use of cellular automaton-like events (precipitations) that transport water down the line of steepest descent and modifies the topography according to a fluvial sediment transport rule and a diffusive hillslope rule. When operating on crustal length scales, this and other models cannot resolve low-order drainages or individual hillslopes. Operating on a grid with cell size L , the hillslope diffusivity becomes an effective diffusivity that must be scaled by L^2 in order to be compared with measured or theoretically derived diffusivities. Beaumont *et al.* [1992] describe a coupled tectonic-geomorphic process model at the mountain range scale that incorporates both fluvial and hillslope processes. Kooi and Beaumont [1994] apply a similar model to the tectonic rifting environment. The resulting topographies are impressive, and one may explore fruitfully a range of geomorphic and tectonic questions. They also admit that the subgrid processes are not resolved and that these are therefore taken into account by an enhanced diffusivity that must scale with the square of the grid cell size.

The present model differs from these predecessors by incorporating a simple subgrid analytical solution for the hillslope shapes, from which the local relief and mean altitude within a grid cell are calculated. I have shown, through a subsidiary analysis of response times of hillslopes to changes in the basal boundary conditions (channel incision), that hillslopes in this environment can be represented by their steady state form. The resulting local relief is scaled by the real (field measurable) diffusivity, the hillslope lengths, and the local incision rate of the channel.

Another cost of the inability to resolve first-order drainages is that I must assign a hillslope length scale. The model cannot

resolve the convergent topography above channel heads, which occur at sites of landscape instability due to shallow landsliding or overland flow processes [Montgomery and Dietrich, 1988; Dietrich *et al.*, 1992, 1993] (see also Willgoose *et al.* [1991]). Then both climate and lithologic information is embedded in this choice of hillslope length, which sets the values of the stability thresholds in the landscape.

Plan view drainage system. If the goal is to address a specific landscape, whose topography, exhumation, relief, etc., will be used to assess the choices of model parameters, one must adopt a strategy that will allow individual drainages to occur in their correct places. In the absence of this strategy, we must depend upon statistical representations of the resulting landscape (e.g., its hypsometric curve, averages of river profiles, and the like), which although useful (Figure 18) are less robust as tests. In addition, the latter approach calls for numerous realizations of the model topography in order to create a statistical basis for comparison with the actual topography. I have taken the former approach and have dictated the planview drainage pattern. The topography rises above sea level with effectively no relief but with a drainage pattern lightly etched into it (adjacent cells are "told" the direction they are to drain in the first time step, as well as their drainage area). The assumption that this drainage pattern does not deform as the crust upon which it rides translates through the bend is a severe one. In the absence of a model grid that can appropriately deform, this problem will remain intractable. The majority of the drainage pattern deformation will occur while the parcel of crust is within the bend region and will be most radically altered by any discrete fault structures that take up oblique strain. I expect this problem to degrade the present model worst to the east of the SAF, where numerous structures are shown to be active.

No depositional scheme. A further fault of the model at present is that there is no depositional scheme in the current geomorphic rule set. While this does not present a problem on the west slopes of the Santa Cruz Mountains, where almost all sediment derived from the mountains is rapidly swept downcoast via longshore drift and out of the system through Monterey Canyon, this is not the case on the east slope of the mountains.

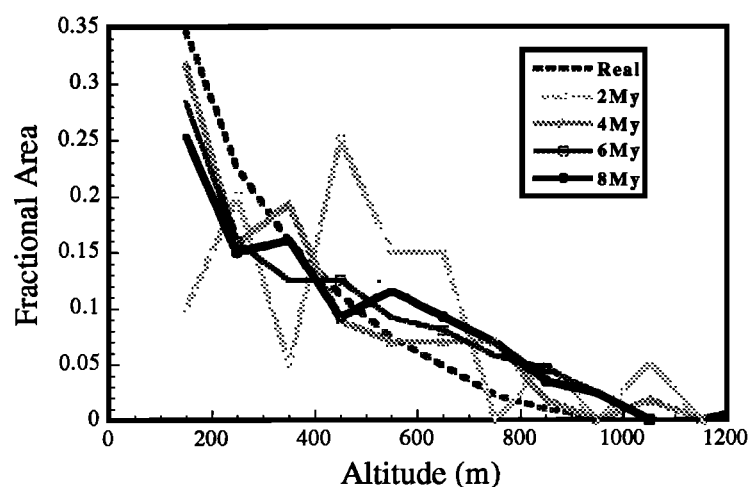


Figure 18. Fractional hypsometry (area in a particular 100 m elevation bin/total land area) for the model topography shown at four evenly spaced intervals up to 3 m.y. in the calculation. The final hypsometry is very similar to that at 6 m.y., implying that steady state topography had developed within approximately 6 m.y. Final hypsometry is similar to that of the present topography (dashed). These elevational statistics of a mountain range topography are potentially important in estimation of the crustal load imposed by ranges of various ages.

This sediment is trapped on alluvial fans on the eastern flank of the mountains, and in the San Francisco Bay, providing a record of deposition and hence of exhumation from the range. This deposit merits further attention as a tracer of the erosional history of the range. A similar fan deposit to the east of San Francisco Bay has been used to great advantage on a shorter, 700 kyr, timescale to deduce climatic fluctuations in sediment output from the Diablo Range [Kolterman and Gorelick, 1992].

Conclusions

I have shown that the hypothesis that the Santa Cruz Mountains may be attributed to uplift associated with a long-lived restraining bend in the San Andreas Fault remains viable under the closer scrutiny of this numerical model. This places constraints on the kinematics of such a fault bend. Alternative models in which the range is due solely to uplift associated with transpressive plate motions must explain the strong (but not perfect) symmetry of the range about the SAF bend.

Not surprisingly, the scale of this particular mountain range is insufficient to trigger significant plate flexure, which in turn disallows the interesting feedback of uplift driven by the geomorphic creation of topographic relief. Nonetheless, the model elements are in place that would allow this feedback to occur given the proper tectonic driving.

Following Koons [1989], I recognize the importance of channel incision as the driving force behind the etching of the topography. Channel incision into bedrock is at the core of the natural evolution of mountain ranges, as it is in this model. It dictates the general pattern of relief and timing of relief production within a range, yet is a process about which we know the least within the suite of geomorphic processes discussed. This process merits further scrutiny within the geomorphic community.

Extensions of this model strategy could include calculation of the expected gravity field, which can constrain yet more tightly the suite of appropriate model parameters. In addition, such modeling efforts could aid in the choice of appropriate field sites for sampling to document the exhumation pattern within this specific mountain range. The broad alluvial apron on the east flank of the northern Santa Cruz Mountains, west of the San Francisco Bay, represents a key site for derivation of a long-term denudation chronology of the mountain range.

Acknowledgments. This work was partially supported by the Petroleum Research Fund of the American Chemical Society, and by NSF (EAR 9158074). I thank Mike Ellis for many stimulating discussions and J. Gomberg and M. Ellis for sharing the boundary element code and discussion of initial results therefrom. The manuscript has benefited greatly from the persistent and exacting editing of S. P. Anderson and from the critical reviews of S. Ellis, D. Valentine, and G. Tucker.

References

- Ahnert, F., Brief description of a comprehensive three-dimensional process-response model of landform development, *Z. Geomorph. Suppl.*, **24**, 11-22, 1970.
- Anderson, R. S., Evolution of the Northern Santa Cruz Mountains by advection of crust past a San Andreas Fault bend, *Science*, **249**, 397-401, 1990.
- Anderson, R. S., and N. F. Humphrey, Interaction of weathering and transport processes in the evolution of arid landscapes, in *Quantitative Dynamic Stratigraphy*, edited by T. A. Cross, pp. 349-361, Prentice Hall, Englewood Cliffs, N.J., 1989.
- Anderson, R. S., and K. M. Menking, The Santa Cruz marine terraces: Evidence for two coseismic uplift mechanisms, *Geol. Soc. Am. Bull.*, **106**, 649-664, 1994.
- Anderson, R. S., D. L. Orange, and S. Y. Schwartz, Implications of the October 17, 1989 Loma Prieta earthquake for the emergence of marine terraces along the Santa Cruz coast, and for long-term evolution of the Santa Cruz Mountains, in *Geology and Tectonics of the Central California Coast Region, San Francisco to Monterey*, edited by R. E. Garrison et al., pp. 205-228, Los Angeles Basin Geological Society, American Association of Petroleum Geologists, Bakersfield, Calif., 1990.
- Andrews, D. J., and R. C. Bucknam, Fitting degradation of shoreline scarps by a nonlinear diffusion model, *J. Geophys. Res.*, **92**, 12,857-12,867, 1987.
- Andrews, D. J., and T. C. Hanks, Scarp degraded by linear diffusion: inverse solution for age, *J. Geophys. Res.*, **90**, B12, 10193-10208, 1985.
- Beaumont C., P. Fullsack, and J. Hamilton, Erosional control of active compressional orogens, in *Thrust Tectonics*, edited by K. McClay, Allen Unwin, London, pp.1-18, 1992.
- Begin, Z. B., Application of a diffusion-erosion model to alluvial channels which degrade due to base-level lowering, *Earth Surf. Processes Landforms*, **13**, 487-500, 1988.
- Best, T. C., and G. B. Griggs, A sediment budget for the Santa Cruz littoral cell, California, in *From Shoreline to Abyss*, Spec. Publ., *Soc. Econ. Paleontol. Mineral.* **46**, 35-50, 1991.
- Bilham, R., and P. Bodin, Fault zone connectivity: Slip rates on faults in the San Francisco Bay area, California, *Science*, **258**, 281-284, 1992.
- Bilham, R., and G. King, The morphology of strike-slip faults: Examples from the San Andreas Fault, California, *J. Geophys. Res.*, **94**, 10,204-10,216, 1989.
- Brown, R. D., Jr., Quaternary deformation, in *The San Andreas Fault System, California*, edited by R. E. Wallace, *U.S. Geol. Surv. Prof. Pap.*, **1515**, 83-113, 1990.
- Burgmann, R., R. Arrowsmith, T. Dumitru, and R. McLaughlin, Rise and fall of the southern Santa Cruz Mountains, California, deduced from fission tracks, geomorphology, and geodesy, *J. Geophys. Res.*, this issue.
- Carslaw, H. S. and J. C. Jaeger, *Conduction of Heat in Solids*, 510 pp., Oxford University Press, New York, 1986.
- Chapman, R. H., and C. C. Bishop, Bouguer gravity map of California, San Francisco sheet, scale 1:250,000, Calif. Div. of Mines and Geol., Sacramento, 1968.
- Chappell, J., The geomorphology and evolution of small valleys in dated coral reef terraces, New Guinea, *J. Geol.*, **82**, 795-812, 1974.
- Chase, C. G., Fluvial landsculpting and the fractal dimension of topography, *Geomorphology*, **5**, 39-57, 1992.
- Culling, W. E. H., Analytical theory of erosion, *J. Geol.*, **68**, 336-344, 1960.
- Culling, W. E. H., Theory of erosion on soil-covered slopes, *J. Geol.*, **73**, 230-254, 1965.
- Dietrich, W. E., C. J. Wilson, D. R. Montgomery, J. McKean, and R. Bauer, Erosion thresholds and land surface morphology, *Geology*, **20**, 675-679, 1992.
- Dietrich, W. E., C. J. Wilson, D. R. Montgomery, and J. McKean, Analysis of erosion thresholds, channel networks, and landscape morphology using a digital terrain model, *J. Geol.*, **101**, 259-278, 1993.
- Dunne, T., Stochastic aspects of the relations between climate, hydrology and landform evolution, *Trans. Jpn. Geomorphol. Union*, **12**, 1-24, 1991.
- Gomberg, J., and M. Ellis, Topography and tectonics of the New Madrid seismic zone: Results of numerical experiments using a new three-dimensional boundary element program, *J. Geophys. Res.*, this issue.
- Griggs, G. B., N. A. Rosenbloom, and J. S. Marshall, Investigations and monitoring of ground cracking and landslides initiated by the October 17, 1989 Loma Prieta earthquake, final report to the Army Corps of Engineers, Santa Cruz, California, 1990.
- Hall, T., Holocene history of the San Andreas fault between Crystal

- Springs Reservoir and San Andreas Dam, San Mateo County, California, *Bull. Seismol. Soc. Am.*, **74**, 281-299, 1984.
- Hanks, T. C., R. C. Bucknam, K. R. Lajoie, and R. E. Wallace, Modification of wave-cut and faulting-controlled landforms, *J. Geophys. Res.*, **89**, 5771-5790, 1984.
- Howard, A. D., and G. Kerby, Channel changes in badlands, *Geol. Soc. Am. Bull.*, **94**, 739-752, 1983.
- Howard, A. D., W. E. Dietrich, and M. A. Seidl, Modeling fluvial erosion on regional or continental scales, extended abstract, paper presented at *Chapman Conference on Tectonics and Topography*, Snowbird, Utah, June 1992.
- Irwin, W. P., Geology and plate-tectonic development, in *The San Andreas Fault System*, edited by R. E. Wallace, *U.S. Geol. Surv. Prof. Pap.*, **1515**, 61-82, 1990.
- Iverson, R., and J. J. Major, Groundwater seepage vectors and the potential for hillslope failure and debris flow mobilization, *Water Resour. Res.*, **22**, 1543-1548, 1986.
- Iverson, R. and M. Reid, Gravity-driven groundwater flow and slope failure potential, 1, Elastic effective stress model, *Water Resour. Res.*, **28**, 925-938, 1992.
- King, G. C. P., R. S. Stein, and J. B. Rundle, The growth of geologic structures by repeated earthquakes, 1, Conceptual framework, *J. Geophys. Res.*, **93**, 13,307-13,318, 1988.
- Kolterman, C. E. and S. M. Gorelick, Paleoclimatic signature in terrestrial flood deposits, *Science*, **256**, 1775-1782, 1992.
- Kooi, H., and C. Beaumont, Escarpment evolution on high-elevation rifted margins: Insights derived from a surface processes model that combines diffusion, advection, and reaction, *J. Geophys. Res.*, **99**, 12,191-12,209, 1994.
- Koons, P. O., The topographic evolution of collisional mountain belts: A numerical look at the Southern Alps, New Zealand, *Am. J. Sci.*, **289**, 1041-1069, 1989.
- Lambeck, K., *Geophysical Geodesy, the Slow Deformations of the Earth*, Clarendon, Oxford, 1988.
- Lisowski, M., W. H. Prescott, J. C. Savage, and M. J. Johnston, Geodetic estimate of coseismic slip during the 1989 Loma Prieta, California, earthquake, *Geophys. Res. Lett.*, **17**, 1437-1440, 1990.
- Marshall, G., R. S. Stein, and W. Thatcher, Faulting geometry and slip from coseismic elevation changes: The 18 October 1989 Loma Prieta, California, earthquake, *Bull. Seismol. Soc. Am.*, **81**, 1518-1539, 1991.
- McKean, J. A., W. E. Dietrich, R. C. Finkel, J. R. Southon, and M. W. Caffee, Quantification of soil production and downslope creep rates from cosmogenic ^{10}Be accumulations on a hillslope profile, *Geology*, **21**, 343-346, 1993.
- McLaughlin, R. J., J. C. Clark, and E. E. Brabb, Geologic map and structure sections of the Loma Prieta 7 1/2' quadrangle, Santa Clara and Santa Cruz counties, California. *U.S. Geol. Surv. Open File Rep.* **88-752**, 31pp., 1988.
- McNutt, M., Flexure reveals great depth, *Nature*, **343**, 131, 1990.
- Molnar, P., and P. England, Late Cenozoic uplift of mountain ranges and global climate change: Chicken or egg?, *Nature*, **346**, 29-34, 1990.
- Monaghan, M. C., J. A. McKean, W. E. Dietrich, and J. Klein, ^{10}Be chronometry of bedrock to soil conversion rates, *Earth Planet. Sci. Lett.*, **111**, 483-492, 1992.
- Montgomery, D. and W. E. Dietrich, Where do channels begin?, *Nature*, **336**, 232-234, 1988.
- Nash, D. B., Morphologic dating of degraded normal fault scarps, *J. Geol.*, **88**, 353-360, 1980.
- Orange, D. L., R. S. Anderson, and N. Breen, Submarine canyon spacing: A coupling of geomorphology and hydrology, *GSA Today*, **4**, 29, 36-39, 1994.
- Page, B. M., and D. C. Engebretson, Correlation between the geologic record and computed plate motions for central California, *Tectonics*, **3**, 133-155, 1984.
- Pierce, K. L., and S. M. Colman, Effect of height and orientation (microclimate) on geomorphic degradation rates and processes, late-glacial terrace scarps in central Idaho, *Geol. Soc. Am. Bull.*, **97**, 869-885, 1986.
- Rantz, S. E., Mean annual precipitation and precipitation depth-duration-frequency data for the San Francisco Bay region, California, *U.S. Geol. Surv. Open File Rep.*, **3019-12**, 1971.
- Raymo, M. E., W. F. Ruddiman, and P. N. Froelich, The influence of late Cenozoic mountain building on oceanic geochemical cycles, *Geology*, **16**, 649-653, 1988.
- Reid, M., and R. Iverson, Gravity-driven groundwater flow and slope failure potential, 2, Effects of slope morphology, material properties, and hydrologic heterogeneity, *Water Resour. Res.*, **28**, 939-950, 1992.
- Rosenbloom, N. A. and R. S. Anderson, Hillslope and channel evolution in the Santa Cruz, California land scape, *J. Geophys. Res.*, **99**, 14,013-14,030, 1994.
- Ruddiman, W. F., and J. E. Kutzbach, Forcing of Late Cenozoic northern hemisphere climate by plateau uplift in southern Asia and the American west, *J. Geophys. Res.*, **94**, 18409-18427, 1989.
- Schwartz, S. Y., D. L. Orange, and R. S. Anderson, Complex fault interactions in a restraining bend on the San Andreas Fault, southern Santa Cruz Mountains, California, *Geophys. Res. Lett.*, **17**, 1207-1210, 1990.
- Seidl, M. A., and W. E. Dietrich, The problem of channel erosion into bedrock, *Catena Suppl.*, **23**, 101-124, 1992.
- Shreve, R. L., Statistical law of stream numbers. *J. Geol.*, **74**, 17-37, 1966.
- Stein, R. S., G. C. P. King, and J. Rundle, The growth of geologic structures by repeated earthquakes 2, Field examples of continental dip-slip faults, *J. Geophys. Res.*, **93**, 13319-13331, 1988.
- Tucker, G. E., and R. L. Slingerland, Erosional dynamics, flexural isostasy, and long-lived escarpments: A numerical modeling study, *J. Geophys. Res.*, **99**, 12,229-12,243, 1994.
- Turcotte, D. L., and G. Schubert, *Geodynamics*, 450 pp., John Wiley, New York, 1982.
- Valensise, G., and S. N. Ward, Long-term uplift of the Santa Cruz coastline in response to repeated earthquakes along the San Andreas Fault, *Bull. Seismol. Soc. Am.*, **81**, 5, 1694-1704, 1991.
- Willgoose, G., R. L. Bras, and I. Rodriguez-Iturbe, Results from a new model of river basin evolution, *Earth Surf. Processes Landforms*, **16**, 237-254, 1991.
- Williams, C. R., T. Arnadottir, and P. Segall, Coseismic deformation and dislocation models of the Loma Prieta earthquake derived from Global Positioning System measurements, *J. Geophys. Res.*, **98**, 4567-4578, 1993.
- Working Group on California Earthquake Probabilities (WGCEP), Probabilities of large earthquakes in the San Francisco Bay Region, California, *U.S. Geol. Surv. Circ.* **1053**, 1990.

R. S. Anderson, Department of Earth Sciences, University of California, Santa Cruz, CA 95064. (e-mail: rsand@bagnold.ucsc.edu)

(Received March 29, 1993; revised March 2, 1994; accepted March 14, 1994.)